Development of a millimeter-period rf undulator

Filippos Toufexis* and Sami G. Tantawi
SLAC National Accelerator Laboratory, Menlo Park, California 94025, USA

(Received 26 July 2019; published 23 December 2019)

We present the design of a rf undulator at 91.392 GHz that has a period of 1.75 mm, while the minimum beam aperture seen by the beam is 2.375 mm. To confine the fields inside the undulator a corrugated waveguide is connected through a matching section to a linear taper and a mirror. After the mirror, a Bragg reflector and a matching section are used to reflect back all the fields leaking out of the mirror opening. This undulator requires approximately 1.4 MW for submicrosecond pulses to generate an equivalent K value of 0.1. Transferring such amounts of power at mm-wave frequencies requires overmoded corrugated waveguides, and coupling through irises creates excessive pulsed heating. We have designed a coupling scheme that allows coupling power from a highly overmoded corrugated waveguide to the undulator cavity through the beam pipe without disturbing the undulator fields. This system of the rf undulator and its coupling scheme allows for fast dynamic control of the polarization of the emitted light.

DOI: 10.1103/PhysRevAccelBeams.22.120701

I. INTRODUCTION

Short-period alternatives to traditional permanent magnet undulators are in-vacuum and superconducting magnet-based undulators [1–3], short-period electromagnet-based undulators [4], microfabricated permanent magnet undulators [5], and microfabricated electromagnet undulators [6,7]. However, obtaining a short period using static magnetic field approaches, while maintaining high fields, requires the beam aperture to be smaller than the undulator period. This, in turn, limits the amount of electron beam current that can be transported through the undulator due to wakefields; when high-current beams go through narrow pipes they induce electromagnetic fields that are referred to as wakefields [8]. These wakefields can be longitudinal, which cause energy spread in the bunch, or transverse, which deflect the bunch to the wall. Longitudinal wakefields scale approximately as the inverse square of the beam pipe radius and transverse wakefields scale roughly as the inverse cube of the beam pipe radius.

Another approach to produce short-period undulators is to use oscillating electromagnetic (EM) fields where the electron beam is wiggled by both the electric and magnetic fields. This approach includes inverse Compton scattering sources [9,10], laser-driven dielectric undulators [11–14], and rf or microwave undulators [15–23]. Inverse Compton scattering sources have small and nonuniform undulator strength in the direction of propagation. Because of their extremely small period, the beam energy required to produce extreme ultraviolet (EUV) or soft x-ray radiation is only a few MeV, and handling intense beams at these energies is impractical. Laser-driven dielectric undulators also have very small gaps and therefore are unsuitable for high current beams.

Radio frequency undulators have been experimentally demonstrated by Shintake [15] and Tantawi *et al.* [20]. The former rf undulator operated at 2.856 GHz, the latter at 11.424 GHz, with undulator periods of 5.5 cm and 1.39 cm, respectively. In this work we scaled the rf undulator of Tantawi *et al.* [20] to 91.392 GHz, which results in an undulator period of 1.75 mm and therefore requires substantially lower beam energy to produce the same wavelength. The period is almost an order of magnitude smaller than the 15 mm of the SACLA FEL undulator [24]. We have redesigned the end sections of this undulator to maintain beam apertures on the order of a few millimeters throughout the undulator [22]. We have also designed a mode converter to couple power into the undulator from a low-loss corrugated waveguide [23]. Figure 1 shows the undulator cavity along with the coupling system. This 91.392 GHz undulator requires 1.4 MW of input rf power for an undulator K value of 0.1. Currently, the only available sources of such power at these frequencies are gyrotrons and gyroklystrons with a large superconducting magnet [25–27]. To energize the undulator, we have developed a new concept for compact mm-wave sources [28]. This source can produce power on the order of tens of kilowatts at millimeter frequencies. The dimensions of the interaction circuit are small enough that no magnetic beam focusing is required, and therefore several individual

*ftouf@slac.stanford.edu

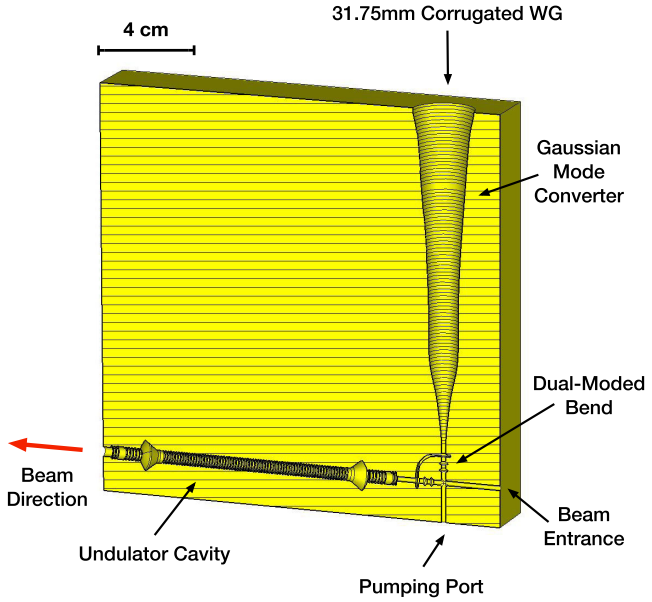

FIG. 1. Millimeter-wave undulator with coupling system cross section, adapted from Toufexis *et al.* [23].

devices could be power combined to produce even more power in a small form factor. Another method to power the undulator is to extract rf power from the drive electron beam [29]. We are currently designing a proof-of-concept EUV light source [30,31] using this approach, reusing most of the existing infrastructure of the SLAC x-band test accelerator [32]. This approach requires the frequency of the undulator to be a harmonic of the SLAC x-band frequency of 11.424 GHz; we have chosen the 8th harmonic that is 91.392 GHz.

Another motivation for this work is the ability to generate light with variable polarization. Conventional undulators produce linearly polarized light. Achieving polarization control in synchrotron light sources and free electron lasers (FELs) is desirable since controlling polarization has applications in the study of magnetic materials [33–35] and biological molecules [36,37], including drugs [38]. Circularly polarized light has been generated in synchrotron light sources using off-plane bending magnet radiation [39] and a variety of insertion devices [40]. Circularly polarized ultraviolet and soft x-ray light has also been generated in FELs [41,42]. Recently a delta undulator [43] was installed in the Linac Coherent Light Source (LCLS) at SLAC to produce even higher energy polarized x-rays [44]. The time required for the LCLS delta undulator to switch polarization between left and right was 35 s [44]. Other methods of producing polarized soft x-rays include high harmonic generation sources [45], which are not efficient in the x-ray regime, and magnetized films [46,47], which are limited to specific wavelengths, low intensity, and achieve only 60% circular polarization.

Axisymmetric rf undulators, such as the rf undulator of Tantawi *et al.* [20] and the one presented in this work, can produce any polarization simply by the user modifying the rf excitation of the undulator cavity. By controlling the rf source, a change of polarization between left and right can be achieved between rf pulses, the spacing of which is typically on the order of milliseconds. This rate of change compares favorably with that of polarization control using phase shifters or a pair of grating polarizer miter bends with motors [48]. In this case, the speed of polarization change is limited by the motors and is takes on the order of a second.

In this work we report the design for an rf undulator at 91.392 GHz. The end sections have been significantly modified from [20] in order to present large beam apertures. In these end sections, a corrugated waveguide is connected through a matching section to a linear taper and a mirror. After the mirror, a Bragg reflector and a matching section are used to reflect back all the fields leaking out of the mirror opening. Power is coupled into this undulator cavity through the beam pipe by a cylindrical $TE_{11}^{\bigcirc}$ mode. Power is transferred to the undulator from a mm-wave source through an overmoded 31.75 mm corrugated waveguide carrying $HE_{11}^{\bigcirc}$ in order to minimize the losses. We used this waveguide because the standard rectangular waveguide WR10 has more than 3 dB m^{-1} attenuation [49], while the 31.75 mm corrugated waveguide has approximately 0.004 dB m^{-1} attenuation [50]. Another reason for interfacing with a 31.75 mm corrugated waveguide is to have a standard vacuum flange. Due to the small dimensions of WR10, it is very difficult to implement a reliable vacuum flange for it. We further report the design of the coupling scheme for the undulator, which preserves the polarization of the input $HE_{11}^{\bigcirc}$ and has large apertures for vacuum pumping and for the electron beam to enter the undulator. The coupling system consists of a Gaussian to cylindrical $TE_{11}^{\bigcirc}$ mode converter and a dual-moded bend. Note that in this work we use $HE_{11}^{\bigcirc}$ and Gaussian TEM_{00} interchangeably. The $HE_{11}^{\bigcirc}$ mode has a maximum 98% similarity with the Gaussian TEM_{00} with a beam waist ratio of 0.64 [51]; the mode converter can be slightly adjusted to achieve either mode. In this work, because we intend to use the mode converter directly with a quasioptical system and not a corrugated waveguide, we have designed it as a Gaussian TEM_{00} to cylindrical $TE_{11}^{\bigcirc}$. Finally we report beam dynamics and synchrotron radiation studies in the undulator, in order to quantify the effect of the new end sections on the radiation spectrum. Parts of this work have been reported in conference format in Toufexis *et al.* [22,23,31].

II. UNDULATOR CAVITY DESIGN

As shown in Fig. 2, the undulator cavity comprises a corrugated waveguide and two end sections. The two end sections form a standing wave within the corrugated waveguide that is the interaction region for the electron beam. The coupling end section couples the cavity to a cylindrical waveguide carrying a $TE_{11}^{\bigcirc}$ mode, while the

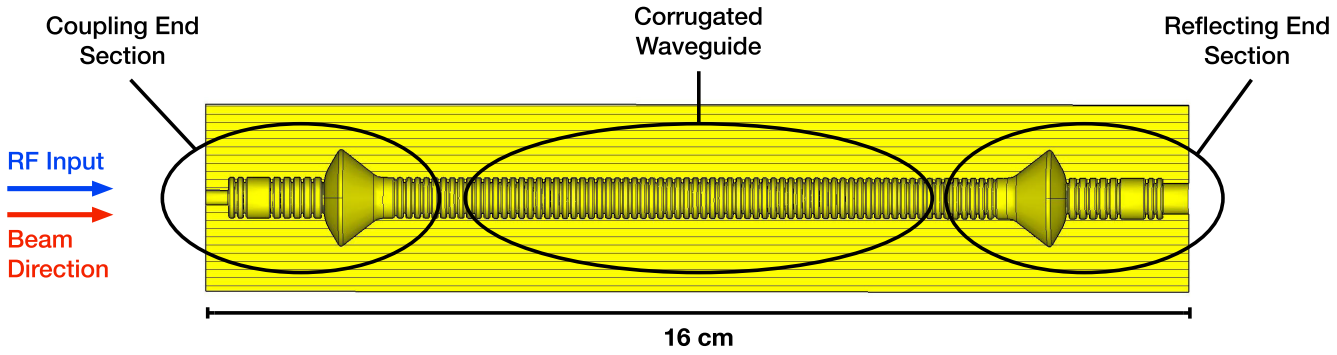

FIG. 2. Millimeter-wave undulator cavity.

reflecting end section acts as a perfect short-circuit. A first-cut design of the end sections and cavity with roundings only at the irises was obtained with a mode matching code similar to the one reported in [52]. Then we re-synthesized the end sections using the same procedure in HFSS with a driven-modal simulation. The frequency, quality factor, and coupling coefficient of a single corrugation period as well as the full undulator cavity were obtained with an eigenmode simulation with HFSS. Here we only report the data of the final HFSS simulations.

A. Corrugated waveguide

The corrugated waveguide dimensions of the body of the undulator are based on scaling the rf undulator of Tantawi *et al.* [20,53]. These dimensions are optimal for an inner corrugated waveguide radius of 3/4 of the rf wavelength. The thickness of the irises of the corrugated waveguide has been doubled from that undulator. The irises are now approximately 400 μm thick and are fully rounded for manufacturability. Figure 3 shows the electric and magnetic field of the unit cell of the corrugated waveguide. As shown in this figure, $HE_{11}^{\circlearrowright}$ has the peak electric and magnetic field on-axis, and both fields are substantially lower at the wall. This allows operation with very high fields in the beam interaction region, with low fields and losses on the metallic walls. The quality factor is 24,700, and the phase advance per unit cell is 134.3 deg. The phase advance per unit cell is reported to give a sense of the relative length of the corrugation period to the wavelength.

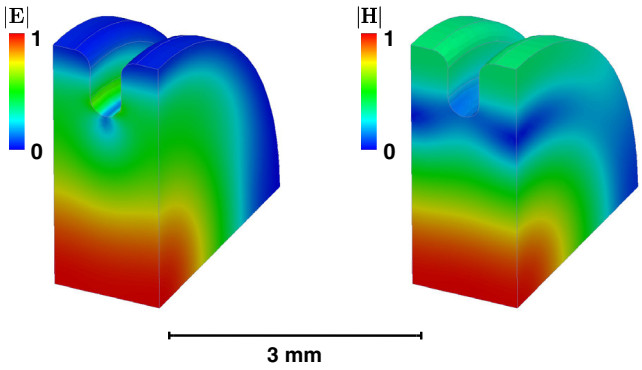

FIG. 3. Surface electric and magnetic field of one quarter of a corrugated waveguide unit cell, adapted from Toufexis *et al.* [22].

B. End section design

Figure 4 shows the new design of the end sections. The purpose of these end sections is to create an rf short-circuit without creating field enhancement at the metallic surface, while preserving apertures at least as large as the corrugated waveguide, which are larger than cutoff. The incident on-axis power density is too large for a simple metallic short circuit; it would melt. To reduce the incident power density to the same level as that at the corrugated waveguide metallic surface, a structure that diffracts the fields away from the center is needed. To create an effective short-circuit without a cutoff hole, a resonant structure that perfectly reflects the incident power density without causing field enhancement on the metallic surface is further required.

To design such end sections, the structure of Fig. 5 is created. A cylindrical waveguide is connected to the corrugated waveguide in order to launch $HE_{11}^{\circlearrowright}$ inside the corrugated waveguide. If the corrugated waveguide were left open at the other end, $HE_{11}^{\circlearrowright}$ would propagate almost like a laser beam, without substantial reduction of the incident power density until very far from the opening. A smooth-walled cylindrical waveguide section is therefore added, as shown in Fig. 5 to cause the field pattern to diffract away from the center. After that, a linear taper with a smooth edge is added. The fields are now guided by the linear taper, and the incident power density on-axis is rapidly reduced. The length of the diffraction section, the radius of the smooth edge, and the angle of the taper are optimized to minimize reflected power while keeping peak fields on the metallic surfaces lower than those on the surface of the corrugated waveguide. The inner radius of the last iris of the corrugated waveguide before the linear taper is larger to reduce the peak field in the final cavity. By modifying this feature, the peak magnetic field in the undulator cavity is reduced by approximately 30%.

Using the field results of the simulation of Fig. 5, a mirror is fitted at the end of the taper. The mirror is a

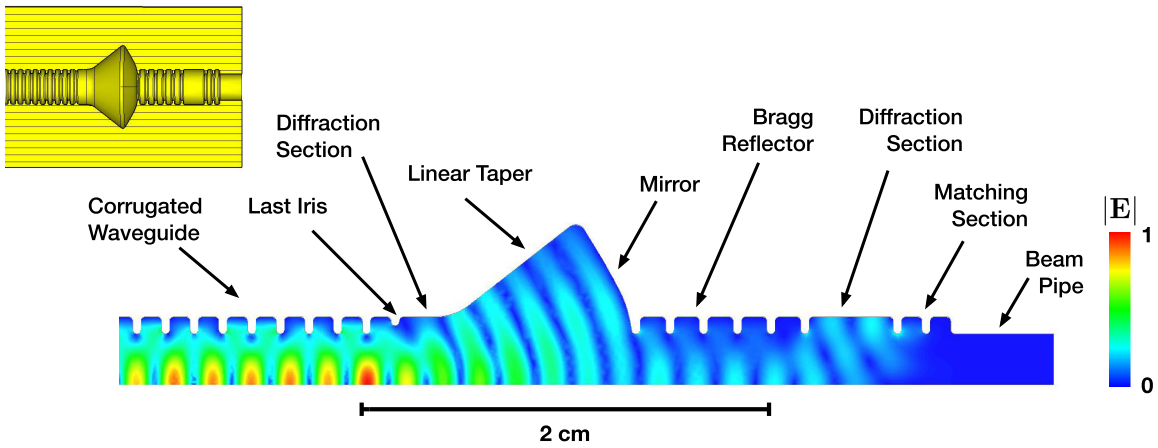

FIG. 4. Surface electric field of the reflective end section—side view. Inset shows the metallic boundary.

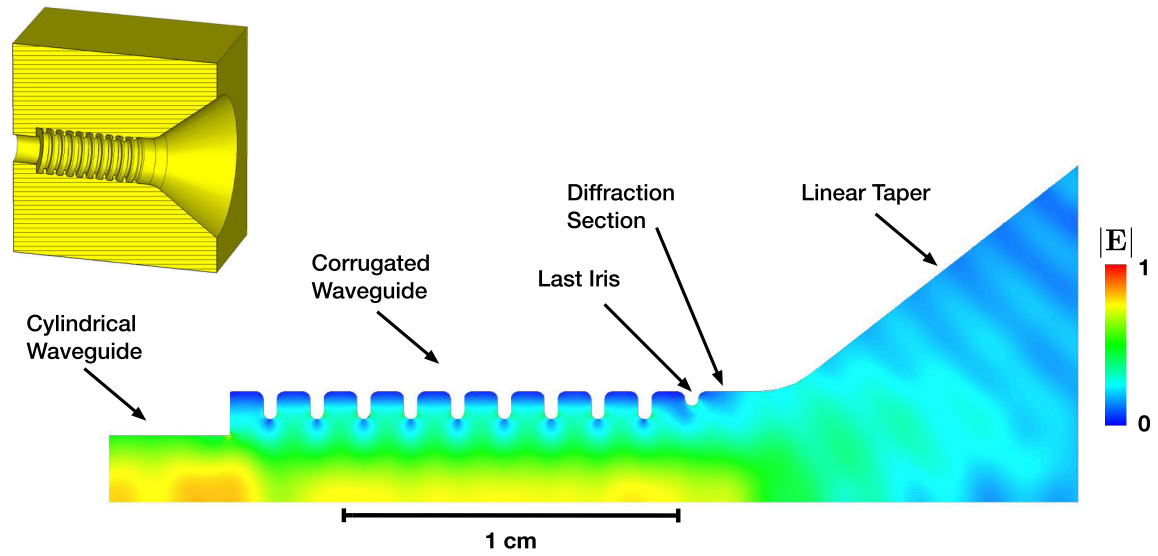

FIG. 5. Surface electric field of the linear taper—side view, adapted from Toufexis *et al.* [22]. Inset shows the metallic boundary.

metallic surface that is fitted in such a way that it is perpendicular to the Poynting vector of the field, and therefore perfectly reflects the incident electromagnetic wave. Algorithm 1 is used to calculate the surface of the mirror. The collection of points obtained with this procedure, shown in Fig. 6, constitutes the surface of the mirror. Note that this is a surface with unique geometry that cannot be fitted in a standard shape like a circle or an ellipse; otherwise the reflected field pattern will not launch the $HE_{11}^{\circlearrowleft}$ mode inside the corrugated waveguide that is the interaction region. The position of the mirror is chosen so that the fields on-axis are approximately the same as those on the surface of the corrugated waveguide. Once the mirror surface is calculated, a hole is created that has the same radius as the inner radius of the corrugated waveguide. The point where the mirror connects to the linear taper is further smoothed, in order to avoid field enhancement.

After the mirror, five periods of a Bragg reflector are used to reflect most of the rf power leaked from the mirror. We implemented a Bragg reflector as a corrugated waveguide, similar to the body of the undulator, that has a period of exactly half a wavelength. The field in a Bragg reflector decays exponentially. The Bragg reflector cannot be used to

Algorithm 1. Mirror fitting algorithm, adapted from Toufexis *et al.* [22].

Input field profile

Start at a point on-axis at the end of the linear taper
while wall of the linear taper is not reached **do**
  At the current point calculate $\mathbf{S} = \frac{1}{2}\mathbf{E} \times \mathbf{H}$
  Calculate $\mathbf{P}$ perpendicular to $\mathbf{S}$, towards positive r
  Calculate point along $\mathbf{P}$, fraction of wavelength away
  Store calculated point in the mirror points list
end while
return list of calculated mirror points

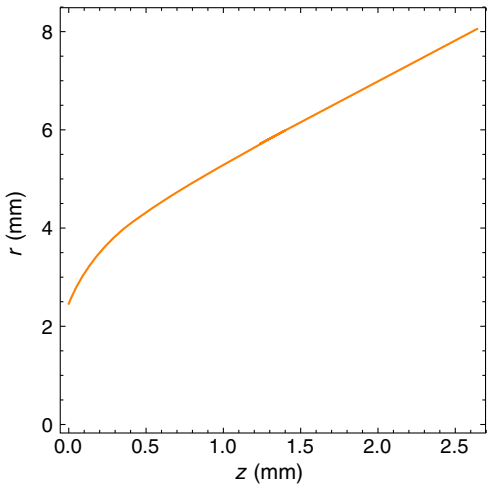

FIG. 6. Surface profile of the mirror.

perfectly reflect all of the power because for it to do so would require too many periods; there is a trade-off between the number of periods and reflection coefficient. We used two more corrugated periods, spaced with a smooth wall waveguide from the Bragg reflector, in order to reflect the remaining power. The length of this smooth walled cylindrical waveguide controls the coupling to the smooth-walled cylindrical waveguide formed by the beam pipe. These features are shown in Fig. 4. We found that this topology is short enough while being able to perfectly reflect the fields. We also found that a choke caused increased fields compared to our implementation of a Bragg reflector.

We have designed two different end sections for the two sides of the undulator, shown in Figs. 7 and 8. One end section is placed on the side of the undulator that interfaces with the Gaussian-to-$TE_{11}^{\bigcirc}$ mode converter. This end section, referred to as the coupling end section, connects to the cylindrical waveguide of the mode converter and is designed to leak approximately −16.5 dB of power inside the cylindrical waveguide, as shown in Fig. 9(a). This amount of power corresponds to critically coupling to the undulator cavity. Note that in the rf undulator of Tantawi *et al.* [20,53] power was coupled into the cavity through a cutoff iris. Flowing 1.4 MW of power at w-band through a tiny cutoff iris would create very high fields on the iris. Here power is coupled through evanescent fields in a cylindrical waveguide larger than cutoff. The second end section, referred to as the reflecting end section, is connected to a beam pipe with the same radius as the inner radius of the corrugated waveguide and is designed to be perfectly reflecting, as shown in Fig. 10(a). By making the output beam pipe of the second end section as large as possible, we anticipate to reduce the parasitic modes that can be excited by the beam.

This design of the end sections has the advantage of having a large aperture for the beam—2.375 mm for the

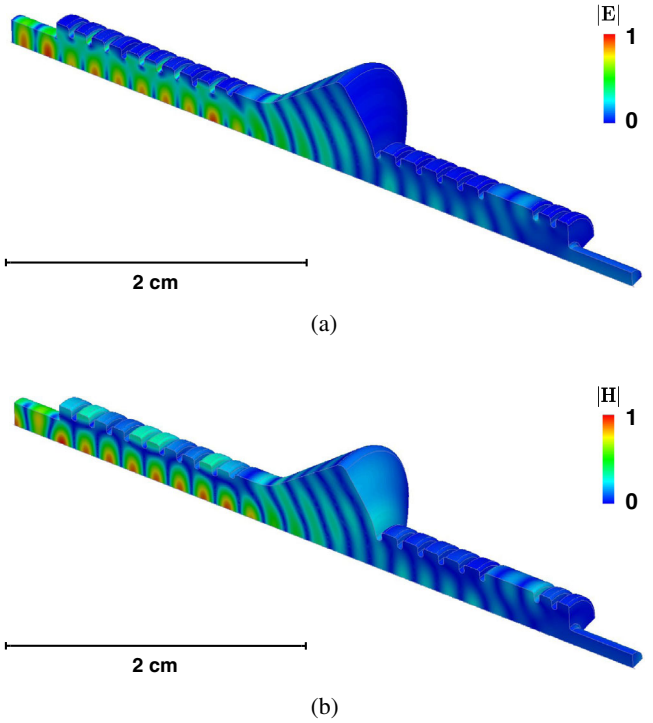

FIG. 7. Surface field profiles of the Coupling End Section, adapted from Toufexis *et al.* [22]. (a) Electric field and (b) magnetic field.

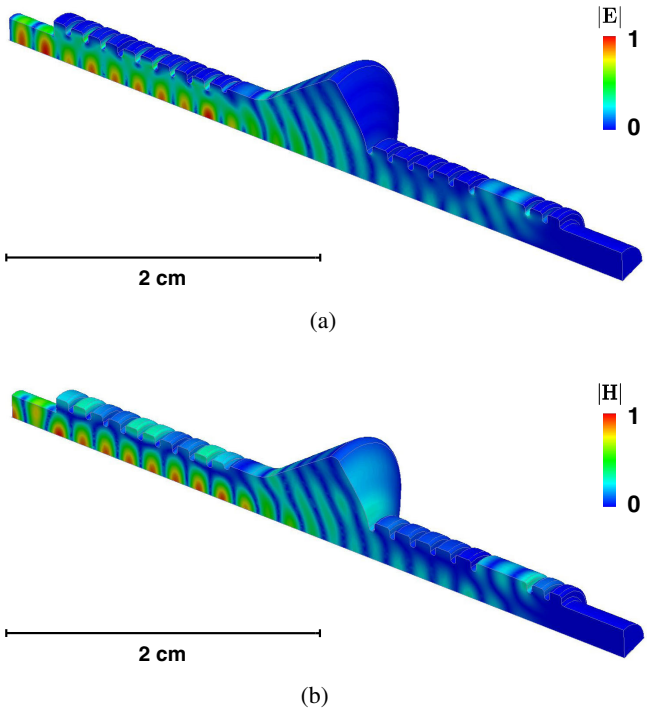

FIG. 8. Surface field profiles of the reflecting end section, adapted from Toufexis *et al.* [22]. (a) Electric field and (b) magnetic field.

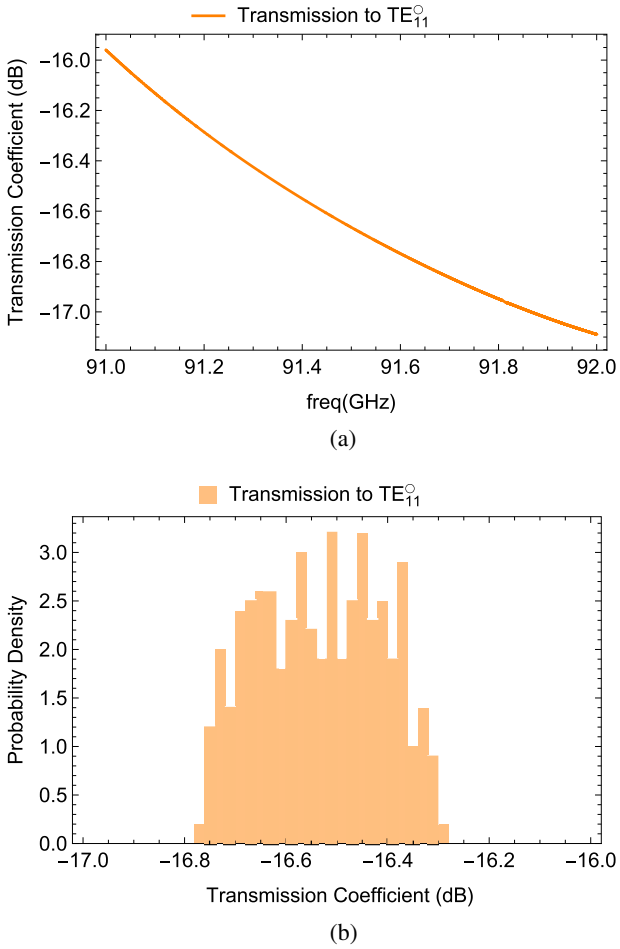

FIG. 9. Coupling end section transmission to the beam pipe. Note that only TE°_{11} can propagate in the beam pipe of the coupling end section. (a) Transmission coefficient of the coupling end section vs frequency and (b) transmission coefficient of the coupling end section tolerances, obtained by varying 4 geometrical parameters uniformly ± 5 μm.

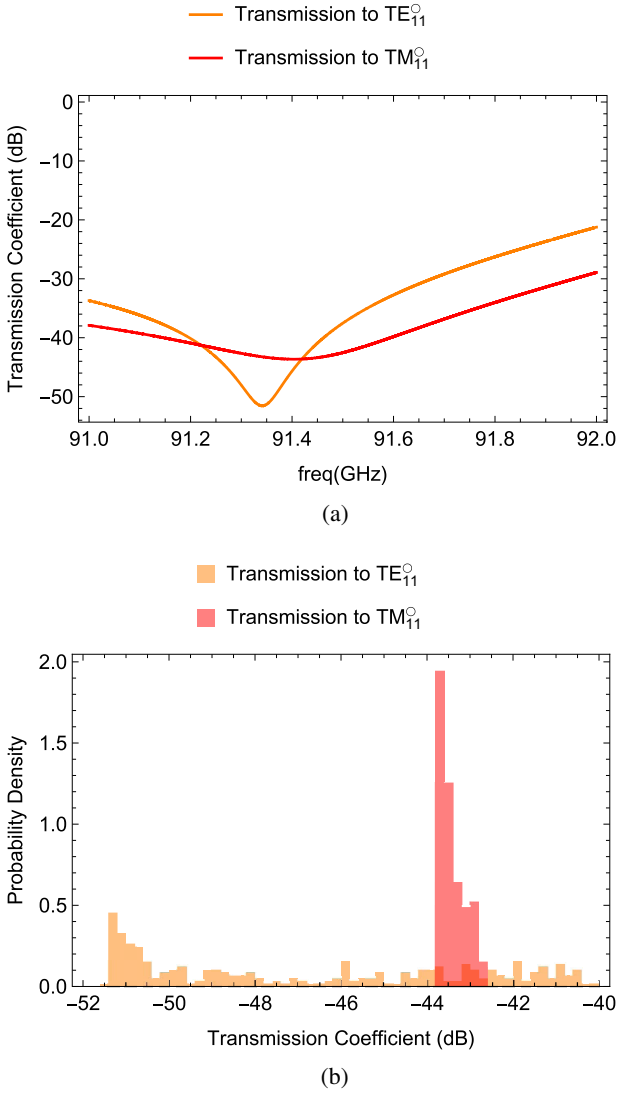

FIG. 10. Reflecting end section transmission to the beam pipe. Note that both TE°_{11} and TM°_{11} can propagate in the beam pipe of the reflecting end section. (a) Transmission coefficient of the reflecting end section vs frequency and (b) transmission coefficient of the reflecting end section tolerances, obtained by varying 4 geometrical parameters uniformly ± 5 μm.

coupling end section and 4.92 mm for the reflecting end section—while being broadband. In the final undulator cavity, the resonance frequency of the mode of interest is mainly affected by the mirrors. Manufacturing imperfections in the position of the mirrors, which would cause a shift in resonance frequency, can be compensated for by using thermal tuning. To investigate the effect of manufacturing errors on the performance, we did a statistical analysis. We varied 4 geometrical parameters uniformly within ± 5 μm. The results are shown in Figs. 9(b) and 10(b). As shown in Figs. 9 and 10, the transmission coefficient of both end sections varies very little with frequency across 1 GHz and it is relatively insensitive to manufacturing imperfections.

C. Undulator cavity

The rf undulator cavity is formed by connecting the two end sections to the ends of the corrugated waveguide. The exact position of the mirrors is slightly tuned to adjust the resonant frequency. Then the outer diffraction section of the coupling end section is fine-tuned to get the cavity critically coupled to the cylindrical waveguide. Figure 11 shows the entire undulator cavity. The intrinsic quality factor is 25,200, and the total quality factor is 12,700. This total quality factor corresponds to a bandwidth of approximately 7.2 MHz. At 91.392 GHz the frequency drift with temperature is 1.6 MHz $^{\circ}C^{-1}$. For 0.1% amplitude variation inside the cavity, the required temperature stability is 0.1 °C.

Figure 11(d) shows the field profile on the axis of the undulator. The field profile has constant amplitude inside

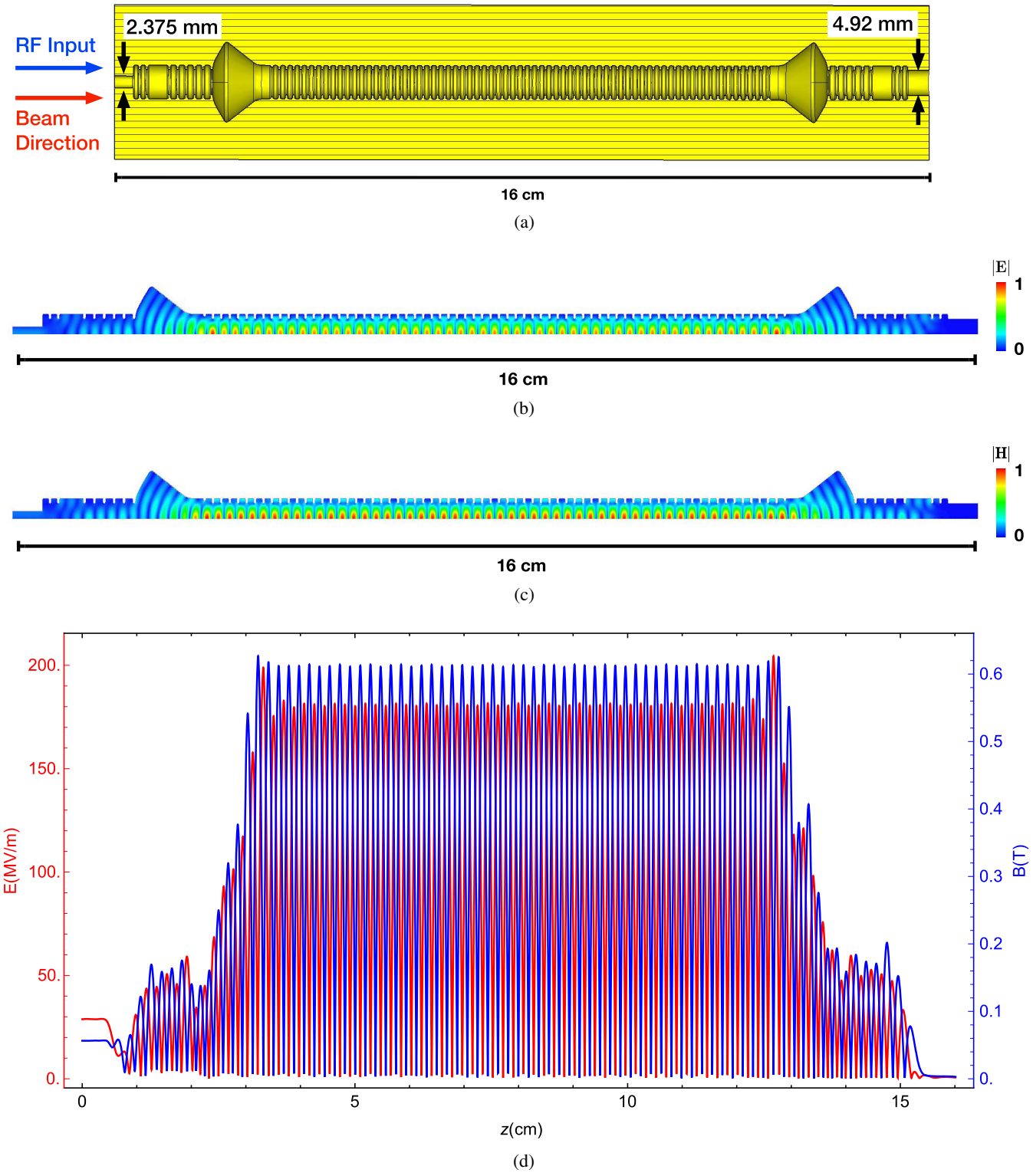

FIG. 11. Undulator cavity, adapted from Toufexis *et al.* [22]. (a) Metallic surface, (b) electric field profile, (c) magnetic field profile, and (d) Undulator cavity on-axis field profile.

the corrugated waveguide and smoothly tapers at the end sections. The undulator period is 1.75 mm, and there are approximately 56 undulator periods inside the corrugated waveguide. The rf power required for $K = 0.1$ is 1.4 MW. The corresponding peak electric and magnetic fields on the metallic surface are 107 MV m^{-1} and 269 kA m^{-1}. For 250 ns rf pulses, the peak pulsed surface heating is 44 °C [54,55], which is considered safe for copper [55]. The rf

power required for $K = 0.15$ is 3.15 MW and the peak pulsed surface heating for 250 ns rf pulses is 99 °C. Operation at this high pulsed surface heating will require hard high-conductivity copper alloys, such as copper-silver [55]. To study the effect of manufacturing errors on the performance, we performed a statistical analysis. We varied 5 geometrical parameters uniformly within ± 5 μm. The results are shown in Fig. 12.

D. Wakefield analysis

Here we present an analysis of the short-range wakes in the rf undulator cavity. The most extreme case is using this rf undulator in compact x-ray FEL and therefore the bunches of interest are extremely short, much smaller than 100 fs rms, and their bandwidth extends to several tens of THz. Performing 3D simulations with that bandwidth is extremely hard in structures that have dimensions of tens of centimeters. Additionally, the effects of the surface resistance at that high frequencies are not well understood. Therefore, to evaluate the wakefield effect of the rf undulator we performed simulations with the axisymmetric code ECHOz2 [56] ignoring the resistive wall for a 100 fs rms bunch ($\sigma_z = 30$ μm), which has a bandwidth on the order of 4 THz. Simulations with shorter bunches, the effects of the resistive wall, and beam dynamics simulations are out of the scope of this paper; we will report on these topics in future publications.

To run ECHOz2 we need the z/r coordinates of the cavity cross-section. We were not able to simulate the exact HFSS geometry with ECHO. The ECHO model has the following differences compared to the HFSS model: (a) the precise position of the mirrors and their shape is not exactly the same, (b) the fillets at the connection of the mirror and linear taper, connection of the input and output beam pipes, and connection of the mirror to the Brag reflector are missing, and (c) the last irises are identical to the rest of the corrugated waveguide.

The results of the ECHOz2 simulation using 100 fs rms bunch length are shown in Fig. 13. The loss factor is

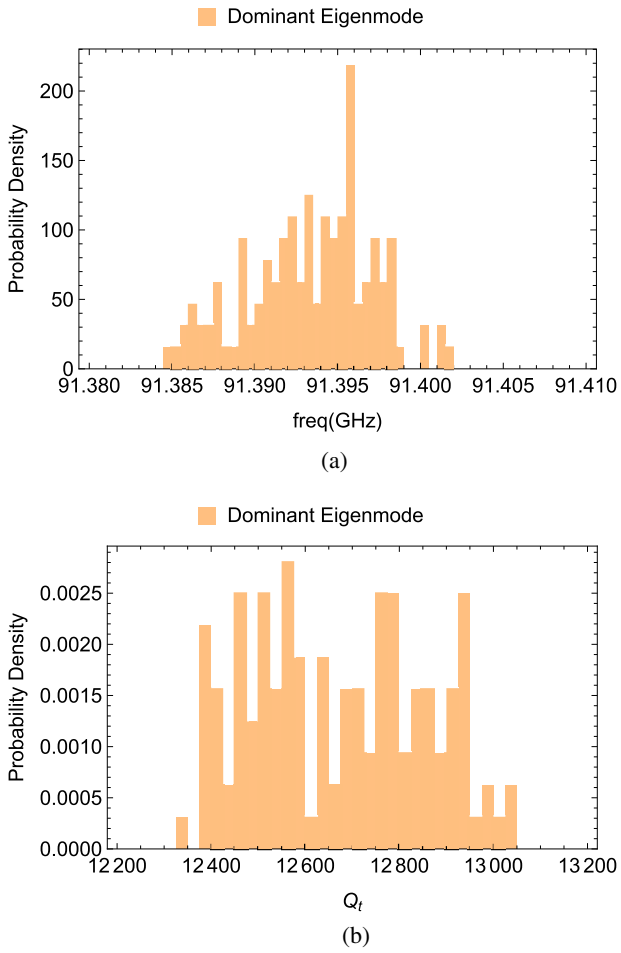

FIG. 12. Cavity eigenfrequency and total quality factor tolerances, obtained by varying 5 geometrical parameters uniformly ± 5 μm. (a) Eigenfrequency tolerances and (b) total quality factor tolerances.

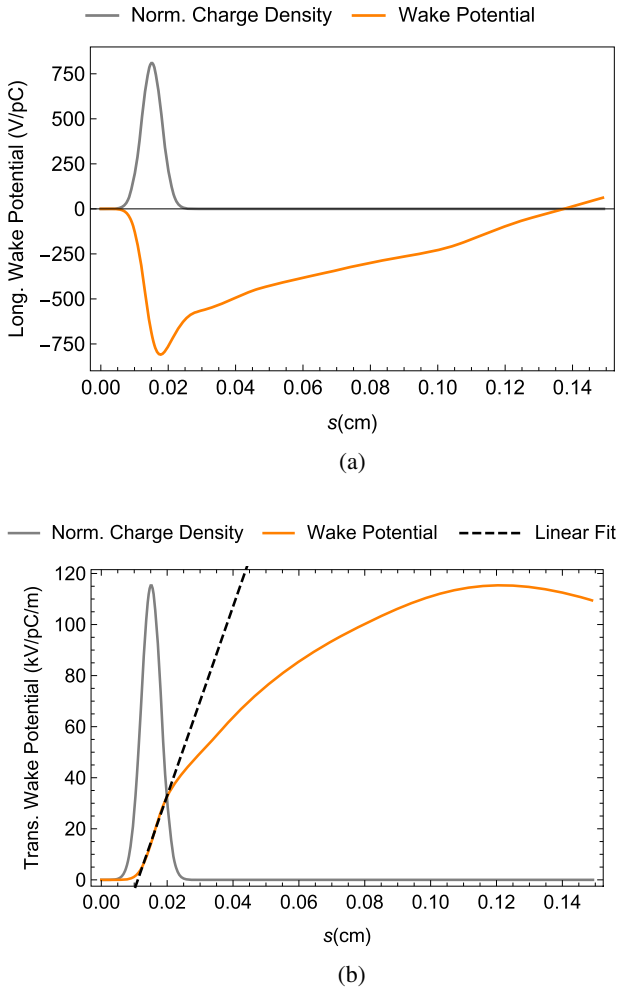

FIG. 13. rf undulator cavity longitudinal and transverse wakefields from a 100 fs bunch, calculated with ECHOz2. (a) Longitudinal wakefield and (b) transverse wakefield. Also shown in this figure is a linear fit around the bunch center.

$k_{\parallel}=581\,\mathrm{V\,pC^{-1}}$ and the kick factor is $k_{\perp}=14.5\,\mathrm{kV\,pC^{-1}\,m^{-1}}$. Figure 13(b) also shows a linear fit around the bunch center; the slope is $W_T' = 37\ \mathrm{kV\,pC^{-1}\,cm^{-2}}$. We will subsequently use this slope to slope to estimate the effect of the transverse wake on the beam.

To quantify the effects of the short-range wakes on the phase space of the beam we will make the following assumptions: the beam energy is $E_b = 1.4$ GeV (energy required for 1 Å radiation with this rf undulator), the bunch charge is $Q_b = 10$ pC, the beam goes through $N_u = 20$ rf undulators, and the beta function inside the undulators is $\beta_u = 5$ m. The longitudinal wakes will induce energy spread on the beam. This longitudinal rms energy spread is approximately 47 kV or 0.003% and is considered negligible.

The transverse dipole wakes will induce transverse oscillations on the tail of the bunch; they will not affect slice emittance, but if the tail slices are substantially displaced transversely from the head slices the projected emittance will grow. To quantify this effect we will use the two-particle model of single-bunch beam breakup in a linac [57,58]. We will assume the bunch charge Q_b is split between two point bunches spaced $\Delta z = 2\sigma_z$. According to this model, the oscillation amplitude Δy at the end of the undulators will have grown compared to the initial head offset y_i according to

$$\frac{\Delta y}{y_i} = \frac{|q_e| Q_b \beta_u N_u}{4E_b} W_T' \Delta z, \tag{1}$$

where q_e is electron charge. Plugging in the numbers results in $\Delta y/y_i = 0.004$ that is considered negligible. This was expected since the bunch is really short, and generally dipole wakes are considered to be problem in the case of long bunches. In conclusion, the wakefields are not an issue in this rf undulator.

III. POWER COUPLING DESIGN

In the rf undulator of Tantawi *et al.* [20], rf power was coupled into the cavity from a rectangular waveguide through a cutoff coupling hole. When operating at mm-wave frequencies, power flow on the order of a MW through cutoff holes causes very high fields on the metallic surfaces, leading to excessive pulsed surface heating and rf breakdowns. For this reason, in our new design power is coupled into the undulator through a cylindrical waveguide operating at $\mathrm{TE}_{11}^{\bigcirc}$ modes, which has a substantially larger aperture than a cutoff coupling hole. This cylindrical waveguide is also the beam pipe, and hence an rf structure is needed that "mixes" the rf wave feeding the undulator and the electron beam. Additionally, at mm-wave frequencies rf power is transferred through highly overmoded corrugated waveguides operating at $\mathrm{HE}_{11}^{\bigcirc}$ modes to reduce the rf losses, which are excessive in a standard rectangular waveguide. Therefore a mode converter is needed that converts the $\mathrm{HE}_{11}^{\bigcirc}$ from the rf power line to a mode that is suitable for powering the undulator. There is an additional requirement that the polarization of the input $\mathrm{HE}_{11}^{\bigcirc}$ from the rf power line is transported unaltered inside the undulator in order to be able to control the polarization of the light from the undulator.

In our design we assume that the rf power transport line is perpendicular to the beam axis. An axisymmetric Gaussian-to-$\mathrm{TE}_{11}^{\bigcirc}$ mode converter is used to convert the incident rf power from the rf power line into $\mathrm{TE}_{11}^{\bigcirc}$ preserving the incident polarization, propagating perpendicular to the beam axis. We designed an rf structure, which we refer to as the dual-moded bend, that accepts this input $\mathrm{TE}_{11}^{\bigcirc}$ mode perpendicular to the beam axis and converts it into a $\mathrm{TE}_{11}^{\bigcirc}$ mode propagating along the beam axis and directly feeds the rf undulator. The dual-moded bend preserves the polarization from its input to its output. Chokes are used to create apertures for the beam to enter the system. The sequence of mode conversions in this coupling system is schematically illustrated in Fig. 14. The dual-moded bend we report here has been modified from the one we reported in Toufexis *et al.* [23]. The position of certain roundings has been changed to allow the structure to be machined in two halves. Additionally the chokes have been redesigned to be elliptical and not have parallel surfaces to avoid multipacting. The data reported here were obtained from HFSS driven-modal simulations.

A. Gaussian-to-TE_{11} mode converter design

The Gaussian-to-$\mathrm{TE}_{11}^{\bigcirc}$ mode converter is used to convert a Gaussian TEM_{00} mode from a corrugated cylindrical waveguide to a smooth-walled cylindrical waveguide $\mathrm{TE}_{11}^{\bigcirc}$.

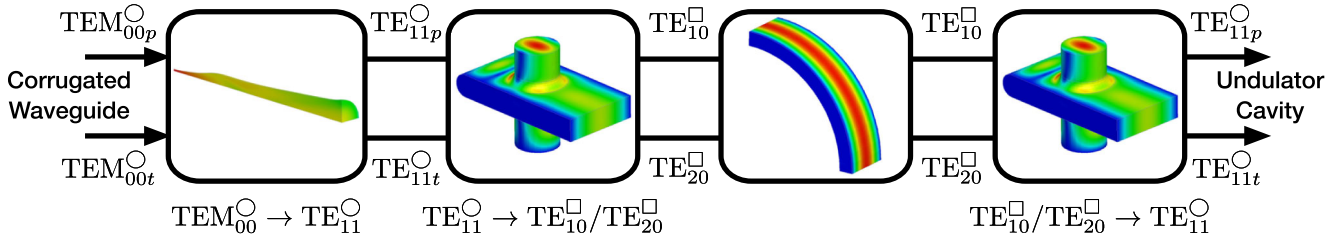

FIG. 14. Coupling system schematic, adapted from Toufexis *et al.* [23].

The smooth cylindrical waveguide is sized to only support $TE^{\bigcirc}_{11}$. This mode converter is axisymmetric, and therefore the two polarizations, $TEM^{\bigcirc}_{00p}$ and $TEM^{\bigcirc}_{00t}$, of the Gaussian mode convert to the equivalent polarizations in the cylindrical waveguide $TE^{\bigcirc}_{11p}$ and $TE^{\bigcirc}_{11t}$. Figure 15 shows the Gaussian-to-$TE^{\bigcirc}_{11}$ mode converter. The complex Gaussian coupling factor is 0.99, the cross-polarization level is −23 dB, the Gaussian beam waist is 0.94 cm, and the reflection coefficient from the cylindrical waveguide is 0.0028. This mode converter was synthesized using a mode matching code [52] and the algorithm described in [59]. At the Gaussian side of this mode converter there will be a vacuum window, to isolate the vacuum system of the undulator from that of the rf transport lines.

B. Dual-moded bend design

To rotate 90 deg the propagation of the $TE^{\bigcirc}_{11}$ coming from the Gaussian-to-$TE^{\bigcirc}_{11}$ mode converter, the two polarization of the incident $TE^{\bigcirc}_{11}$ are converted into the $TE^{\square}_{10}$ and $TE^{\square}_{20}$ in a rectangular waveguide. Figure 16 shows this mode converter. The rectangular waveguide is sized to only support $TE^{\square}_{10}$ and $TE^{\square}_{20}$. The cylindrical $TE^{\bigcirc}_{11p}$ is converted to the rectangular $TE^{\square}_{10}$ and the cylindrical $TE^{\bigcirc}_{11t}$ is converted to the rectangular $TE^{\square}_{20}$, where the subscripts "p" and "t" refer to parallel and transverse with respect to the symmetry plane of the mode converter. Figure 17 shows the s-parameters of this mode converter versus frequency.

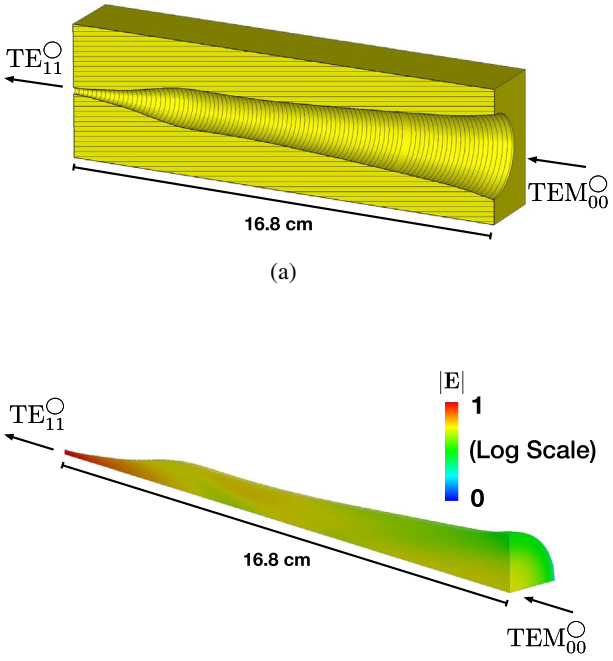

FIG. 15. Gaussian-to-$TE^{\bigcirc}_{11}$ mode converter, adapted from Toufexis *et al.* [23]. (a) Metallic surface and (b) Surface electric field profile (log scale).

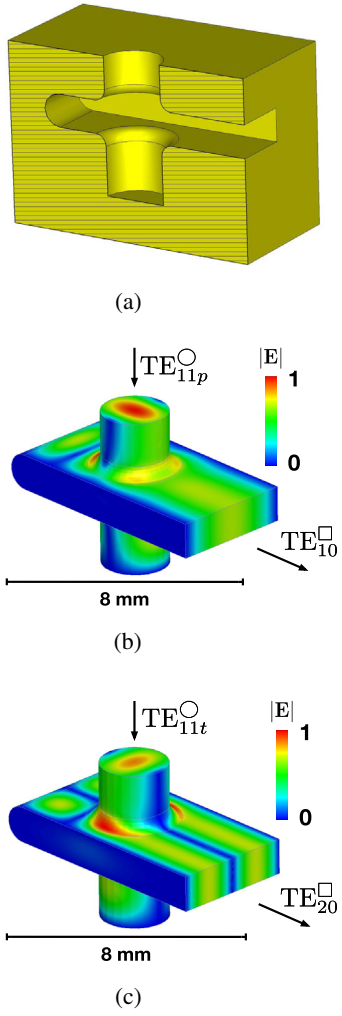

FIG. 16. $TE^{\bigcirc}_{11}$-to-$TE^{\square}_{10}/TE^{\square}_{20}$ mode converter, adapted from Toufexis *et al.* [23]. (a) Metallic surface, (b) surface electric field for the parallel polarization, and (c) surface electric field for the transverse polarization.

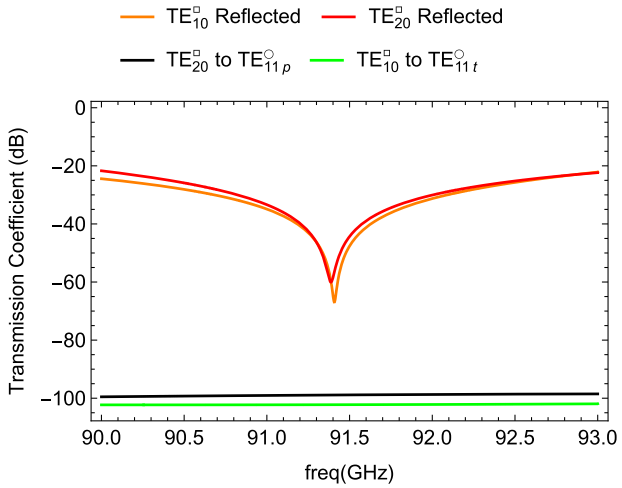

FIG. 17. Cylindrical $TE^{\bigcirc}_{11}$ to rectangular $TE^{\square}_{10}/TE^{\square}_{20}$ mode converter s-parameters vs frequency.

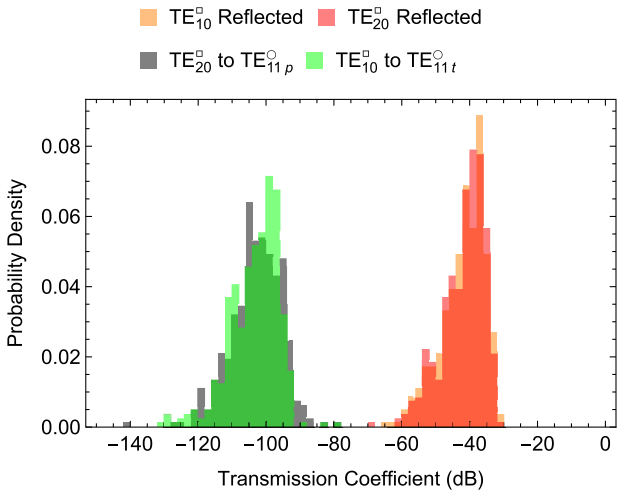

FIG. 18. Cylindrical $TE^{\bigcirc}_{11}$ to rectangular $TE^{\square}_{10}/TE^{\square}_{20}$ mode converter s-parameters tolerances, obtained by varying 7 geometrical parameters uniformly ± 5 μm.

To investigate the effect of manufacturing errors on the performance, we performed a statistical analysis. We varied 7 geometrical parameters uniformly within ± 5 μm. The results are shown in Fig. 18. The mode converter is not significantly affected under these assumptions.

Subsequently, the $TE^{\square}_{10}$ and $TE^{\square}_{20}$ are transported through an E-plane rectangular bend, as shown in Fig. 19. If the radius of the bend is large enough compared to the dimension of the cross-section of the waveguide, the modes propagate unreflected. At the end of the rectangular bend a second $TE^{\bigcirc}_{11}$-to-$TE^{\square}_{10}/TE^{\square}_{20}$ mode converter converts the $TE^{\square}_{10}$ and $TE^{\square}_{20}$ into the two polarizations of $TE^{\bigcirc}_{11}$. Now the axis of propagation of the output $TE^{\bigcirc}_{11}$ has been rotated by 90 deg. This sequence of mode conversions is schematically illustrated in Fig. 14.

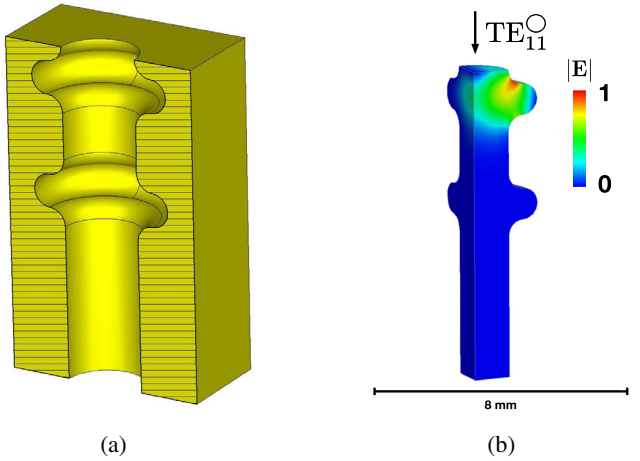

(a) (b)

FIG. 20. $TE^{\bigcirc}_{11}$ double choke. (a) Metallic surface and (b) surface electric field.

The bottom of the mode converter of Fig. 16(a) needs to be physically open for the electron beam to go through. To create an opening in the metal that behaves as a rf short circuit we used a pair of chokes, shown in Fig. 20. A choke is a resonant structure that acts as a rf short circuit. We investigated using both a single choke and a double choke. Figure 21 shows the s-parameters of the two cases versus frequency. We used chokes here instead of a Bragg reflector since it is easier to get perfect reflection with two chokes than with a Bragg reflector. Additionally, since this is a transmission network, field enhancement is not as big of an issue as in the undulator cavity. To study the effect of manufacturing errors on the performance, we performed a statistical analysis. We varied 5 geometrical parameters for the single choke and 6 for the double choke uniformly within ± 5 μm. The results are shown in Fig. 22. As shown in Figs. 21 and 22, the double choke is much more

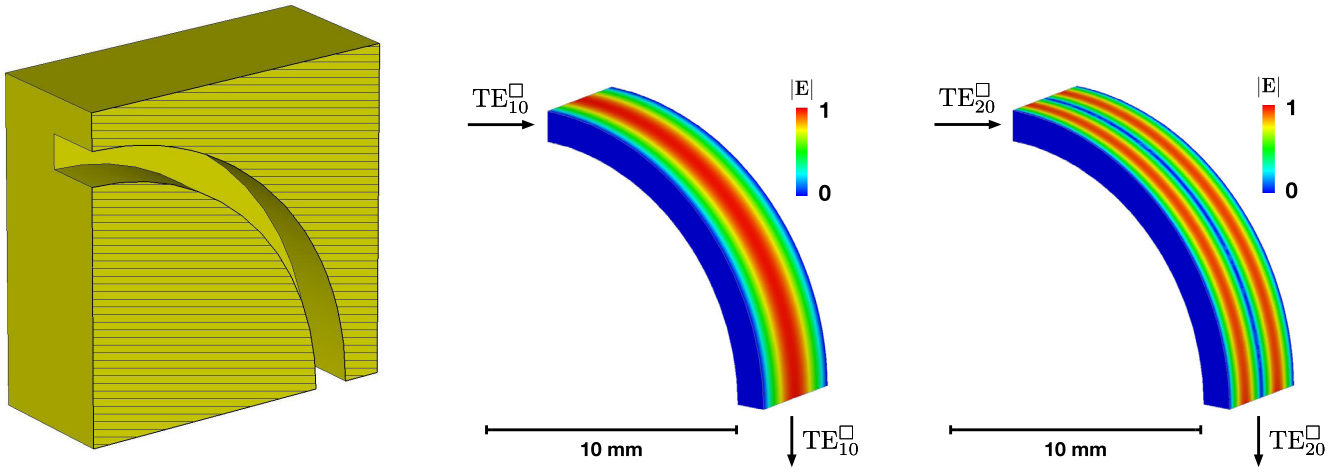

(a) (b) (c)

FIG. 19. $TE^{\square}_{10}/TE^{\square}_{20}$ bend. (a) Metallic surface, (b) surface electric field for the $TE^{\square}_{10}$, and (c) Surface electric field for the $TE^{\square}_{20}$.

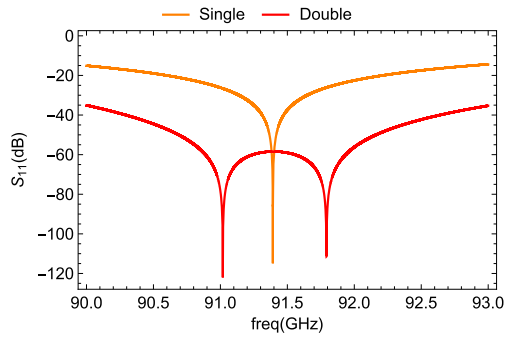

FIG. 21. Single vs double choke reflection vs frequency.

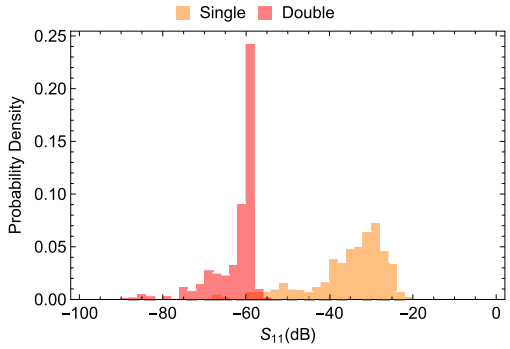

FIG. 22. Single vs double choke reflection tolerances, obtained by varying 5 geometrical parameters for the single choke and 6 geometrical parameters for the double choke uniformly ± 5 μm.

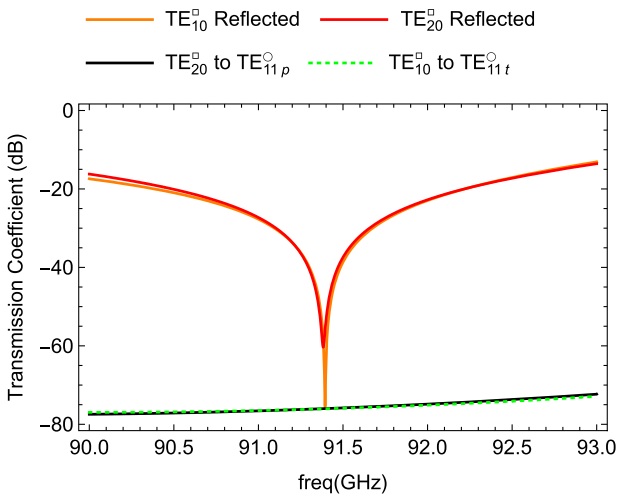

FIG. 24. Cylindrical $TE^{\bigcirc}_{11}$ to rectangular $TE^{\square}_{10}/TE^{\square}_{20}$ mode converter with chokes s-parameters vs frequency.

broadband and less sensitive to manufacturing tolerances than the single choke.

The chokes of Fig. 20 are assembled with the mode converter of Fig. 16(a). The exact position of the chokes with respect to the mode converter is retuned. The result is shown in Fig. 23. Figure 24 shows the s-parameters of the mode converter with the chokes versus frequency. To study the effect of manufacturing errors on the performance, we

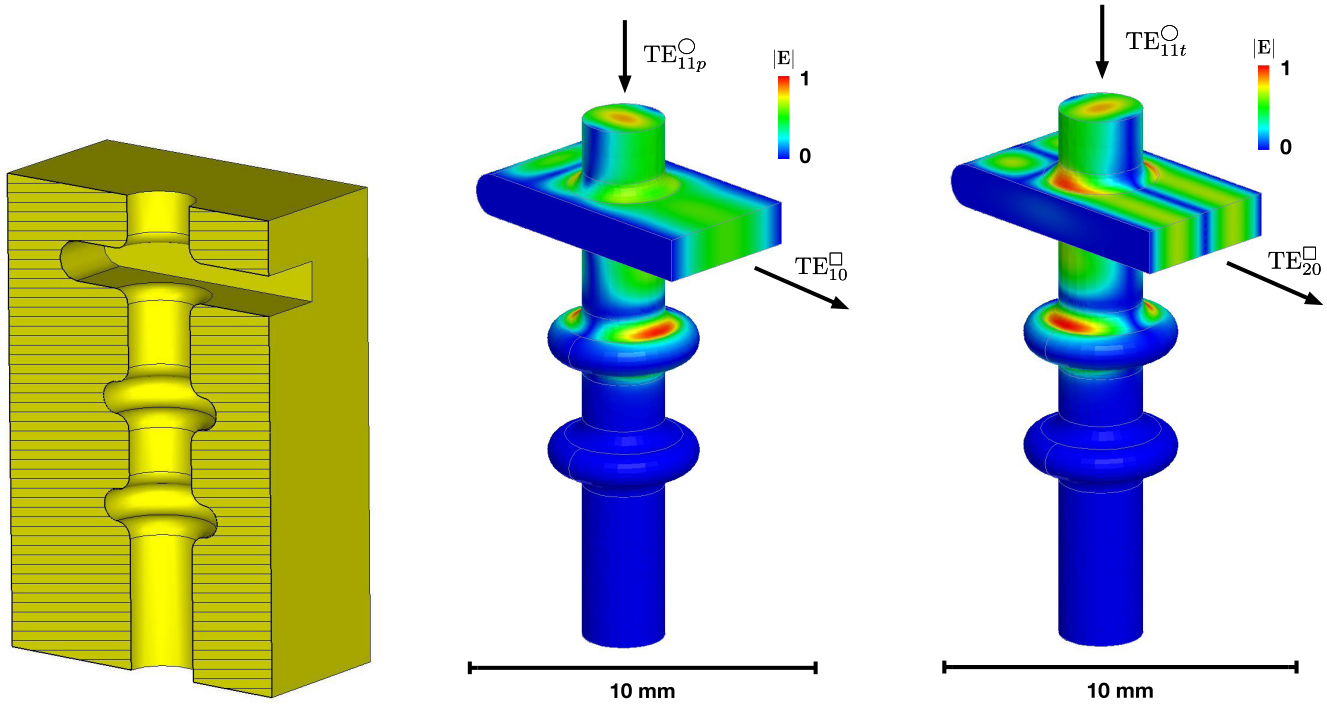

(a) (b) (c)

FIG. 23. $TE^{\bigcirc}_{11}$ to rectangular $TE^{\square}_{10}/TE^{\square}_{20}$ mode converter with chokes. (a) Metallic surface, (b) surface electric field for the parallel polarization, and (c) surface electric field for the transverse polarization.

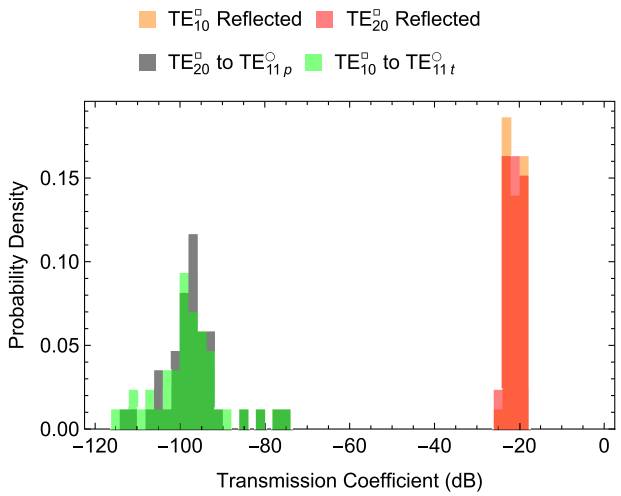

FIG. 25. Cylindrical $TE^{\bigcirc}_{11}$ to rectangular $TE^{\square}_{10}/TE^{\square}_{20}$ mode converter with chokes s-parameters tolerances, obtained by varying 11 geometrical parameters uniformly ± 5 μm.

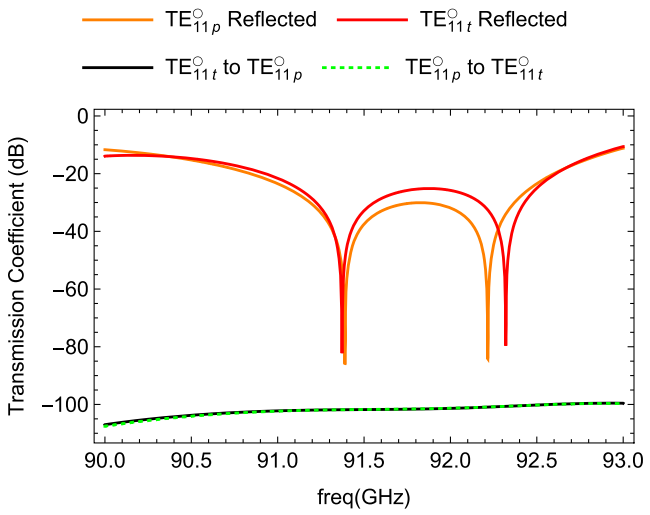

FIG. 27. Dual-moded bend s-parameters vs frequency.

performed a statistical analysis. We varied 11 geometrical parameters uniformly within ± 5 μm. The results are shown in Fig. 25. The mode converter is affected by the geometrical errors, however, it is still operational. Note that varying 11 geometrical parameters simultaneously and uniformly is a very extreme case. Also, modern precision CNC machines can achieve tolerances of ± 3 μm.

Figure 26 shows the complete dual-moded bend. The distance between the two cylindrical $TE^{\bigcirc}_{11}$ to rectangular $TE^{\square}_{10}/TE^{\square}_{20}$ mode converters and the rectangular E-plane bend is fine-tuned so that there is no phase slippage between the two polarizations of $TE^{\bigcirc}_{11}$ at the end of the dual-moded bend. As can be seen in Fig. 26, each polarization of $TE^{\bigcirc}_{11}$ at the input cylindrical waveguide is transmitted unaltered to the output cylindrical waveguide. The use of chokes allows for two orthogonally placed through holes, one for the electron beam to enter the undulator, and one to pump the vacuum space of the mode converter. Figure 27 shows the s-parameters of the dual-moded bend versus frequency. For a 10 MW power flow through this mode converter, the peak magnetic field on the metal surface is 282 kA m^{-1}. From [54] the peak pulsed surface heating for 250 ns rf pulses is 48 °C, which is considered safe for copper [55]. Figure 1 shows the entire system assembly with the undulator.

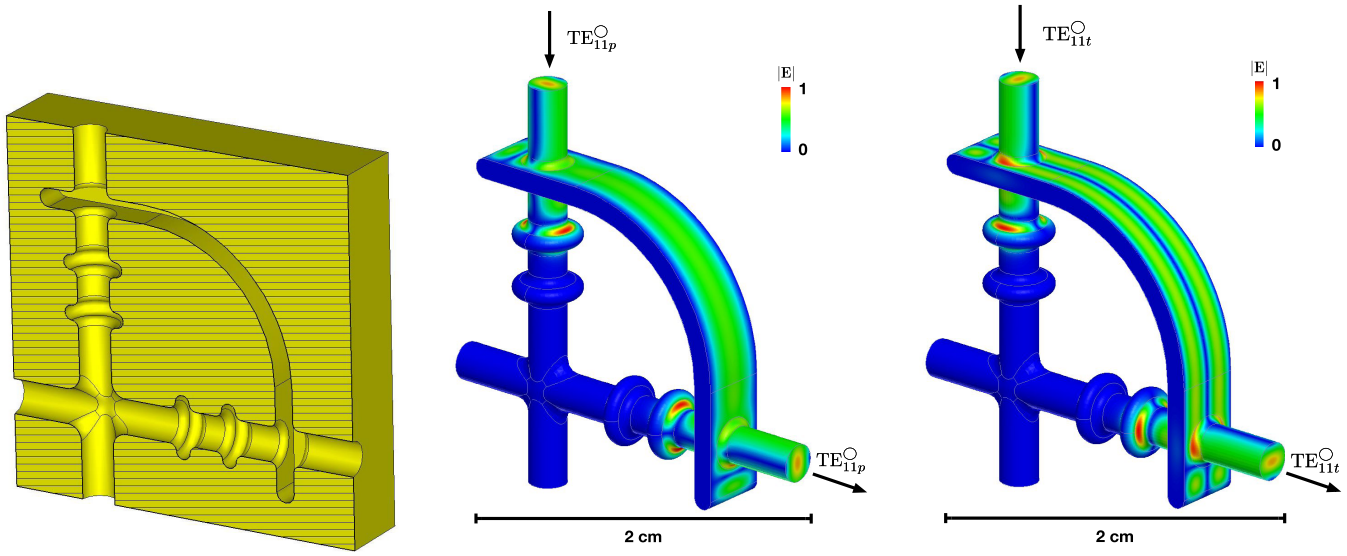

(a) (b) (c)

FIG. 26. Dual-moded bend, adapted from Toufexis *et al.* [23]. (a) Metallic Surface, (b) surface electric field for the parallel polarization, and (c) surface electric field for the transverse polarization.

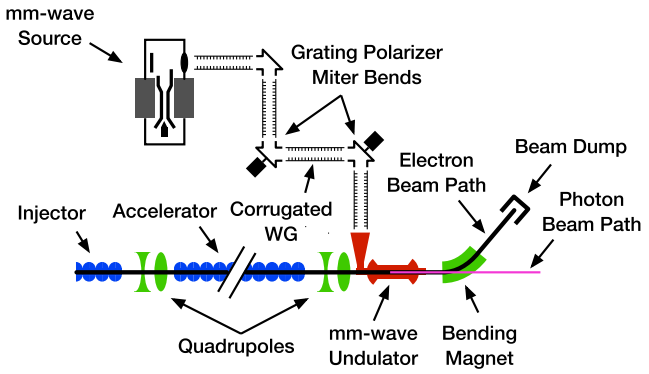

FIG. 28. Light source schematic utilizing the mm-wave undulator with polarization control, adapted from Toufexis *et al.* [23,31].

C. Polarization control

Polarization of the produced light is directly controlled by the polarization of the Gaussian mode incident to the undulator system of Fig. 1. $TE_{11}^{\circlearrowright}$ gyro traveling wave tubes such as the one reported in [60–62] could be modified to produce variable polarization by having two input signals separately coupled to the two polarizations of the $TE_{11}^{\circlearrowright}$. A change of polarization between left and right could be achieved between rf pulses, the spacing of which is typically on the order of milliseconds.

Typically such a source is not readily available. An alternative method to control and change the polarization is the use of a pair of grating polarizer miter bends with motors [48]. In this case, the speed of polarization change is limited by the motors and is on the order of a second. Figure 28 shows the schematic of a light source utilizing the mm-wave undulator with polarization control.

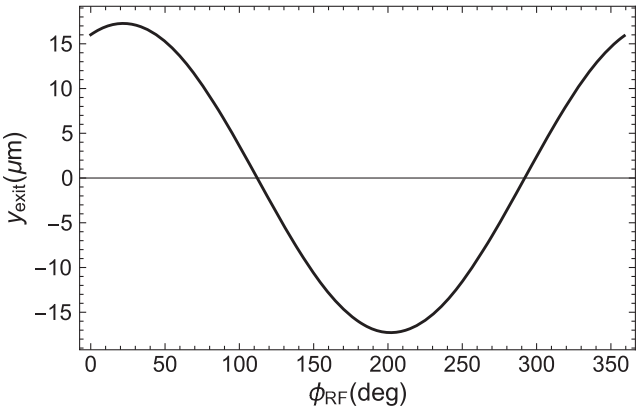

FIG. 30. Beam drift at the exit of the undulator versus rf injection phase, adapted from Toufexis *et al.* [31].

IV. SYNCHROTRON RADIATION FROM THE RF UNDULATOR

Since we have redesigned the end sections of the rf undulator, we need to investigate their effects on the beam dynamics and synchrotron radiation spectrum. As discussed by Shintake [15], when an electron beam interacts with a guided copropagating and a counterpropagating deflecting EM wave, the equivalent undulator period λ_u is given by

$$\lambda_u = \frac{\lambda_0}{1 \pm \frac{\lambda_0}{\lambda_G}}, \tag{2}$$

where λ_0 is the free space wavelength, and λ_G is the waveguide wavelength. The plus sign corresponds to the EM wave counterpropagating with the electrons, and the minus sign corresponds to the EM wave copropagating

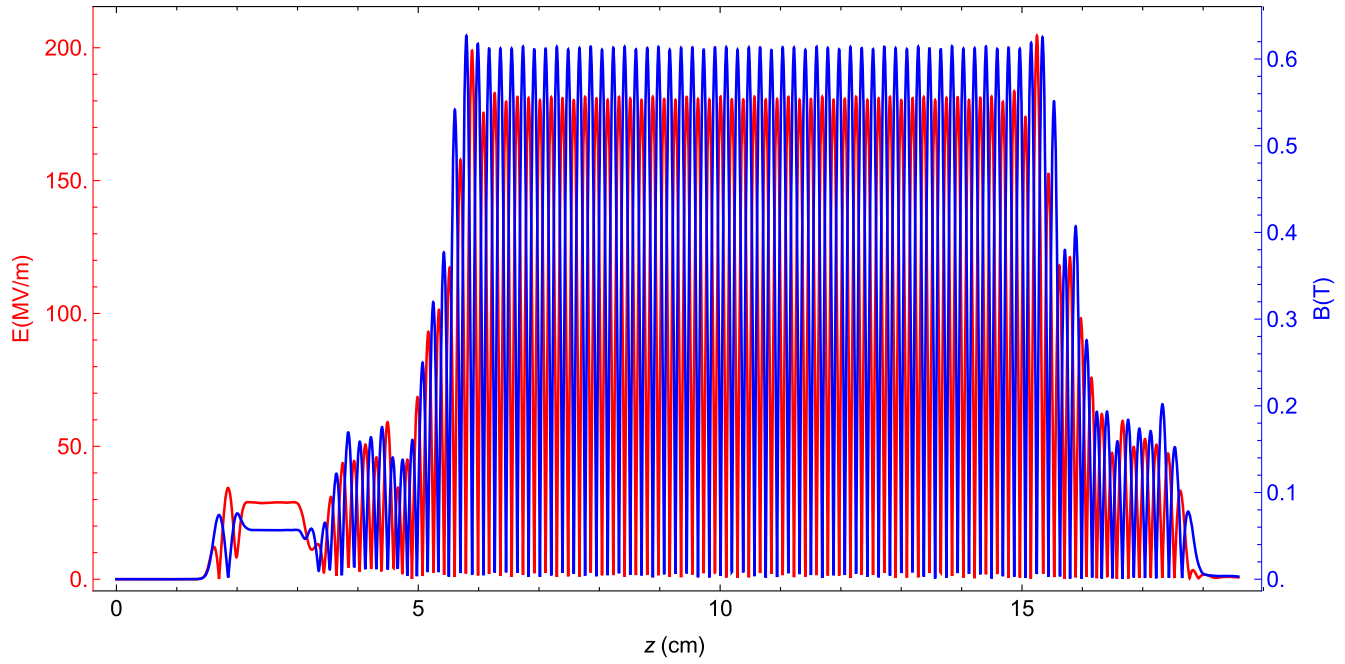

FIG. 29. Radio frequency undulator cavity on-axis field profile with the dual-moded bend, adapted from Toufexis *et al.* [31].

with the electrons. These two cases are referred to as short-period and long-period undulation, respectively. In the rf undulator presented here, the short-period is 1.75 mm and the long-period is 2.66 cm. In the rf undulator cavity, the standing wave can be decomposed into a copropagating and a counterpropagating EM wave, hence both short and long-period undulation mechanisms are present. Depending on the rf phase of the cavity fields when the beam is injected, the long-period undulation may cause the beam to drift. The oscillating EM fields in the rf undulator can be described by an equivalent static magnetic field [21] $B_{x,eq}$ given by

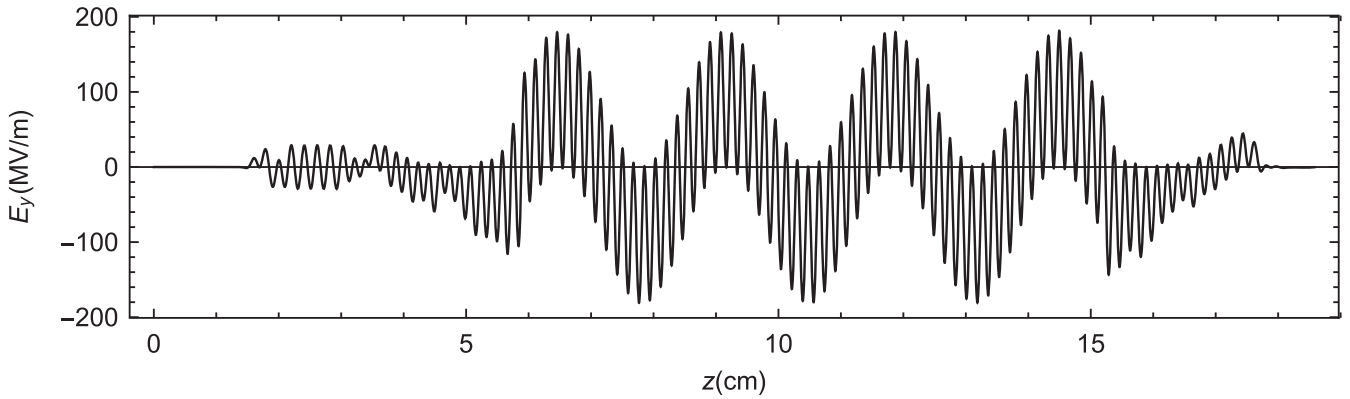

(a)

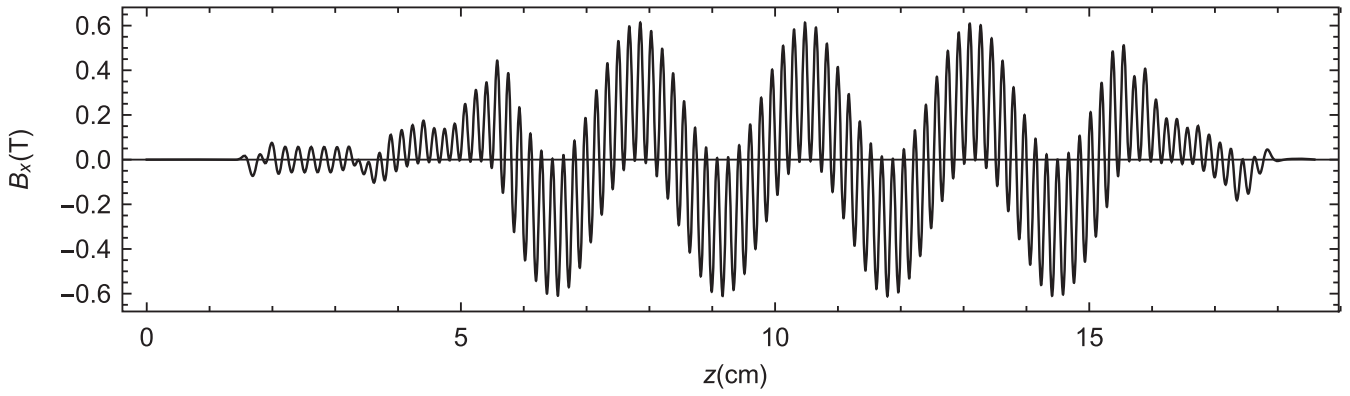

(b)

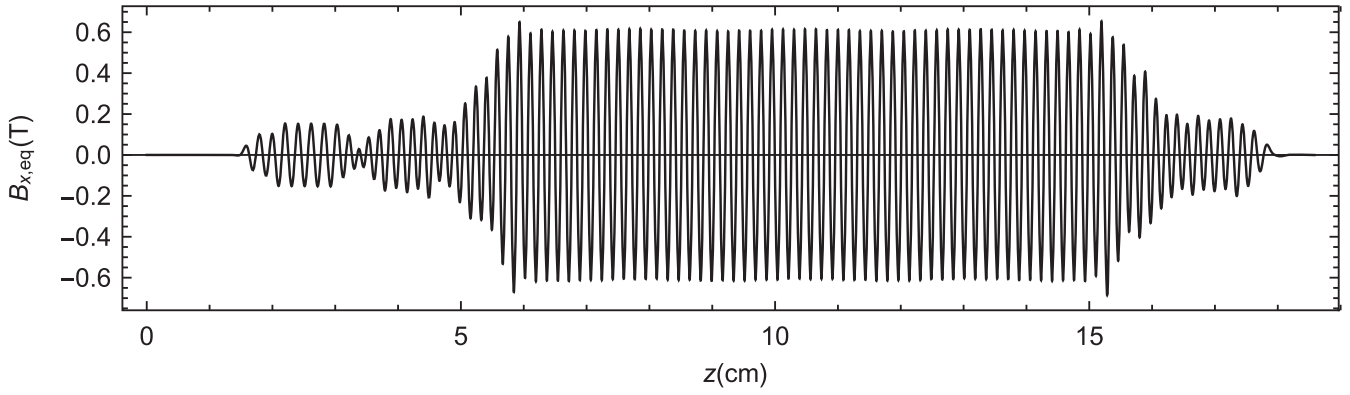

(c)

FIG. 31. Fields seen by the electron beam when injected with $\phi_{rf} = 112$ deg, adapted from Toufexis *et al.* [31].

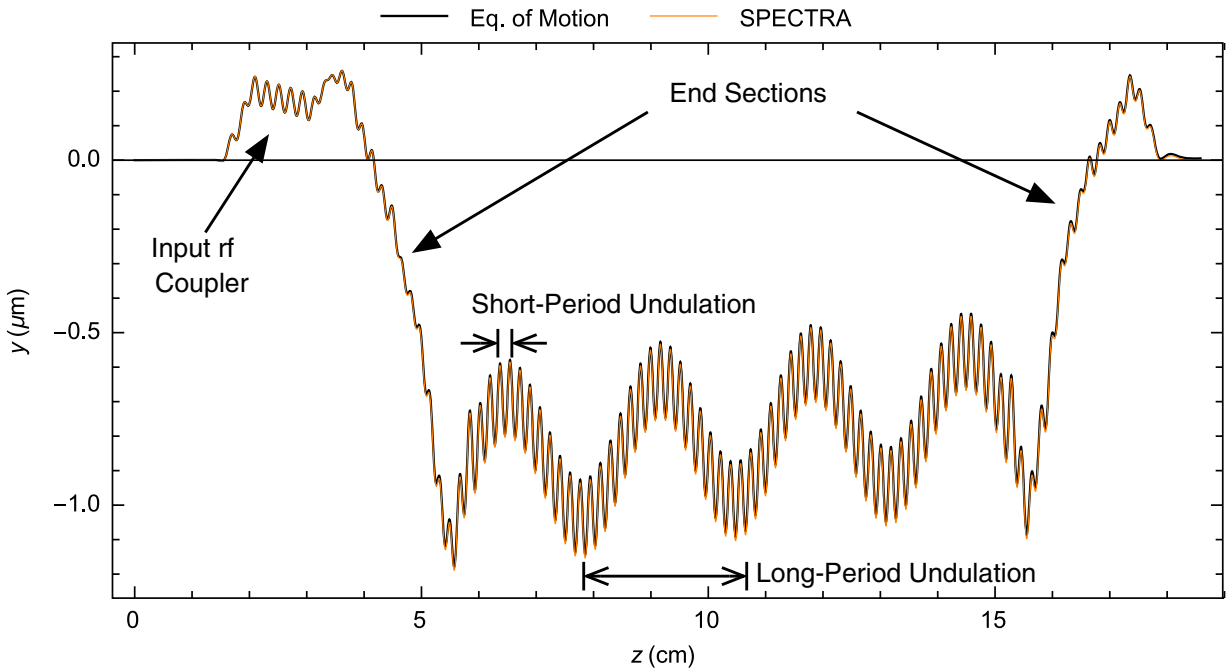

FIG. 32. Single electron orbit inside the rf undulator for $K = 0.1$, adapted from Toufexis *et al.* [31]. The black curve was obtained by solving the equations of motion using time varying electric and magnetic fields. The orange curve was obtained from SPECTRA simulation using the equivalent undulator fields.

$$B_{x,eq}(z,\phi_{rf}) = \Re\left\{\left[\mathbf{B}_x + \frac{\mathbf{E}_y}{c}\right] e^{j\left(\frac{z\omega_{rf}}{\beta c}+\phi_{rf}\right)}\right\}, \qquad (3)$$

where $\mathbf{B}_x = \mathbf{B}_x(z)$ and $\mathbf{E}_y = \mathbf{E}_y(z)$ are the on-axis complex magnetic and electric field obtained from eigenmode simulation of the cavity, c is the speed of light, $\omega_{rf} = 2\pi f_{rf}$, f_{rf} is the resonant frequency of the undulator, β is the ratio of the electron velocity to the speed of light, and ϕ_{rf} is the rf injection phase.

To evaluate the electron beam drift due to the long-period undulation, we performed beam dynamics simulations for different rf phases. For these simulations we combined the field profile of the undulator cavity and the dual-moded bend, as shown in Fig. 29. The results of the beam dynamics simulations are shown in Fig. 30. This figure was obtained by solving the equations of motion using the complex on-axis fields of Fig. 29, which correspond to $K = 0.1$. The maximum drift is small compared to the beam apertures of the undulator and could be corrected by linac beam optics. Figure 31 shows the electric, magnetic, and equivalent undulator magnetic field seen by a particle having a beam energy of 129 MeV. The beam is injected at an rf phase of 112 deg, which corresponds to near-zero beam drift.

For synchrotron radiation calculation we used SPECTRA [63–65]. SPECTRA has built-in models for permanent magnet undulators, as well as user-defined static magnetic field undulators. To simulate the rf undulator, we used the *user-defined undulator* model with the equivalent undulator magnetic field profile of Fig. 31(c). To validate the correctness of the electron orbit calculated by SPECTRA, we performed single electron beam dynamics simulation with SPECTRA and we also solved the equations of motion in *Mathematica* using the on-axis rf electric and magnetic field. The results are shown in Fig. 32. The two methods indeed produce the same orbit. Figure 32 shows both the short- and long-period undulation, as well as the effects of the newly designed end sections, which cause a substantial local displacement of the beam.

We performed a near-field, energy dependent, spatial flux density calculation, 2 m from the undulator using SPECTRA. We used the bunch parameters of [31]. We further assumed 171,360 bunches per second (250 ns rf pulses, 60 Hz repetition rate). We performed the same calculation using the equivalent undulator magnetic field of the rf undulator and using a 56-period permanent magnet undulator (the same undulator periods as that of the rf undulator). The results are shown in Fig. 33. The 56-period permanent magnet undulator produces lower flux density than the rf undulator. We also performed a simulation using a 62-period permanent magnet undulator. The results are also shown in Fig. 33. The rf undulator and the 62-period permanent magnet undulator produce near identical spectrum around the peak flux density. Each end section behaves as if it had 3 additional periods, but we see a small shift in the spectrum peak upwards in photon energy. We speculate that this shift is because the amplitude and K

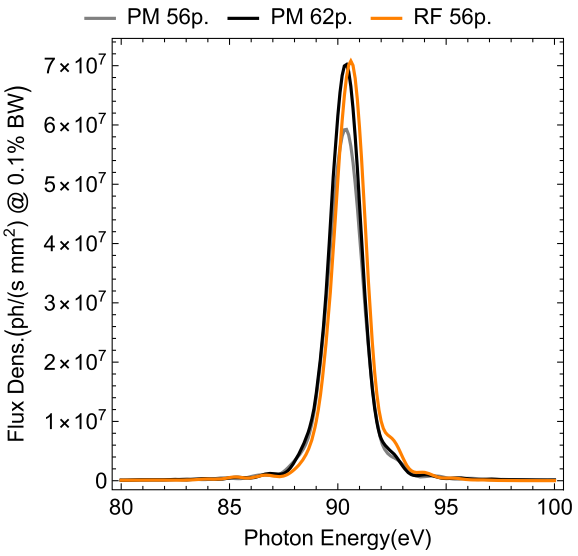

FIG. 33. Comparison of near field spectrum 2 m downstream of the undulator between a permanent magnet undulator of 56 periods, a permanent magnet undulator of 62 periods, and the rf undulator for $K = 0.1$, adapted from Toufexis *et al.* [31].

of these additional periods are lower than those inside the corrugated waveguide. We can conclude that the rf undulator behaves as a static undulator with 6 additional periods.

V. SUMMARY

In this work we reported the design of a short-period rf undulator at 91.392 GHz. The undulator period is 1.75 mm and the beam aperture diameter is 2.375 mm. The required power for $K = 0.1$ is 1.4 MW, and the undulator can operate at that power level for 250 ns for copper. Power is coupled to the undulator through the beam pipe carrying $TE_{11}^{\circlearrowright}$. We investigated the beam dynamics inside the rf undulator and the produced radiation spectrum and found that the end sections have a small effect on the output spectrum.

We further reported the design of a coupling scheme for the undulator at 91.392 GHz. Power is transferred from the mm-wave source through a 31.75 mm corrugated waveguide. The $HE_{11}^{\circlearrowright}$ in the corrugated waveguide is converted into cylindrical $TE_{11}^{\circlearrowright}$, and then bent 90 deg to feed the undulator while preserving polarization. This coupling scheme allows fast change of polarization between left and right on the order of a second using grating polarizers, and on the order of milliseconds through the mm-wave source. By comparison, the time to switch polarization between left and right for the LCLS delta undulator was 35 s [44].

ACKNOWLEDGMENTS

We wish to acknowledge Jeff Neilson for designing the Gaussian mode converter. We further thank Gordon Bowden, Valery Dolgashev, Philipp Borchard, and Diana Gamzina for the fruitful conversation on how to machine the undulator. We wish to thank Karl Bane for reviewing our wakefield calculations. This project was funded by U.S. Department of Energy under Contract No. DE-AC02-76SF00515, and the National Science Foundation under Contract No. PHY-1415437.

[1] T. Tanaka, T. Hara, R. Tsuru, D. Iwaki, X. Marechal, T. Bizen, T. Seike, and H. Kitamura, In-vacuum undulators, in *Proceedings of the 27th International Free Electron Conference* (JACoW, California, USA, 2005), pp. 370–377, http://accelconf.web.cern.ch/accelconf/f05/PAPERS/TUOC001.PDF.

[2] J. Bahrdt and Y. Ivanyushenkov, Short period undulators for storage rings and free electron lasers, J. Phys. Conf. Ser. **425**, 032001 (2013).

[3] Y. Ivanyushenkov, M. Abliz, C. Doose, J. Fuerst, Q. Hasse, M. Kasa, V. Lev, N. Mezentsev, V. Syrovatin, E. Trakhtenberg, V. Tsukanov, I. Vasserman, and E. Gluskin, Development of a superconducting undulator for the APS, J. Phys. Conf. Ser. **425**, 032007 (2013).

[4] S. Yamamoto, A novel attempt to develop very short period undulators, J. Phys. Conf. Ser. **425**, 032014 (2013).

[5] B. A. Peterson, O. D. Oniku, W. C. Patterson, D. Le Roy, A. Garraud, F. Herrault, N. M. Dempsey, D. P. Arnold, and M. G. Allen, Technology development for short-period magnetic undulators, Phys. Procedia **52**, 36 (2014).

[6] J. Harrison, A. Joshi, J. Lake, R. Candler, and P. Musumeci, Surface-micromachined magnetic undulator with period length between 10 μm and 1 mm for advanced light sources, Phys. Rev. Accel. Beams **15**, 070703 (2012).

[7] J. Harrison, A. Joshi, Y. Hwang, O. Paydar, J. Lake, P. Musumeci, and R. N. Candler, Surface-micromachined electromagnets for 100 μm-scale undulators and focusing optics, Phys. Procedia **52**, 19 (2014).

[8] A. W. Chao, *Physics of Collective Beam Instabilities in High Energy Accelerators* (Wiley-VCH, New York, 1993).

[9] R. J. Loewen, A compact light source: Design and technical feasibility study of a laser-electron storage ring x-ray source, Ph.D. thesis, Stanford University, 2003.

[10] W. S. Graves, J. Bessuille, P. Brown, S. Carbajo, V. Dolgashev, K. H. Hong, E. Ihloff, B. Khaykovich, H. Lin, K. Murari, E. A. Nanni, G. Resta, S. Tantawi, L. E. Zapata, F. X. K artner, and D. E. Moncton, Compact x-ray source based on burst-mode inverse Compton scattering at 100 KHz, Phys. Rev. Accel. Beams **17**, 120701 (2014).

[11] T. Plettner and R. L. Byer, Proposed dielectric-based microstructure laser-driven undulator, Phys. Rev. Accel. Beams **11**, 030704 (2008).

[12] A. D. Debus, M. Bussmann, M. Siebold, A. Jochmann, U. Schramm, T. E. Cowan, and R. Sauerbrey, Traveling-wave Thomson scattering and optical undulators for high-yield EUV and X-ray sources, Appl. Phys. B **100**, 61 (2010).

[13] V. Karagodsky and L. Schächter, High efficiency x-ray source based on inverse Compton scattering in an optical Bragg structure, Plasma Phys. Controlled Fusion **53**, 014007 (2011).

[14] F. Toufexis, T. Tang, and S. G. Tantawi, A 200 um-period laser-driven undulator, in *Proc. of the Free-Electron Laser Conference, Basel, Switzerland, Aug. 2014* (JACoW, Geneva, 2014).

[15] T. Shintake, Experimental results of microwave undulator, International Conference on Insertion Devices for Synchrotron Sources **0582**, 336 (1986).

[16] S. Tantawi, V. Dolgashev, C. Nantista, C. Pellegrini, J. Rosenzweig, and G. TravishA coherent Compton backscattering high gain FEL using an X-band microwave undulator, in Proceedings of the 27th International Free Electron Laser Conference, 2005, Stanford, California, USA (2005), http://accelconf.web.cern.ch/Accelconf/f05/PAPERS/THOA006.PDF.

[17] M. Shumail, G. B. Bowden, C. Chang, J. Neilson, S. G. Tantawi, and C. Pellegrini, Application of the balanced hybrid mode in overmoded corrugated waveguides to short wavelength dynamic undulators, Conf. Proc. **C110904**, 3328 (2011).

[18] M. Shumail, G. Bowden, C. Chang, J. Neilson, and S. Tantawi, Beam dynamics studies of a helical X-band RF undulator, AIP Conf. Proc. **1507**, 752 (2012).

[19] C. Chang, J. Neilson, C. Pellegrini, M. Shumail, and S. G. Tantawi, Single electron dynamic of microwave undulator, in *Proc. of International Particle Accelerator Conference (IPAC'12), New Orleans, Louisiana, USA, 20-25 May, 2012* (JACoW, Geneva, Switzerland, 2012), pp. 753–755.

[20] S. Tantawi, M. Shumail, J. Neilson, G. Bowden, C. Chang, E. Hemsing, and M. Dunning, Experimental Demonstration of a Tunable Microwave Undulator, Phys. Rev. Lett. **112**, 164802 (2014).

[21] M. Shumail and S. G. Tantawi, Theory of electromagnetic insertion devices and the corresponding synchrotron radiation, Phys. Rev. Accel. Beams **19**, 074001 (2016).

[22] F. Toufexis and S. G. Tantawi, A 1.75 mm period RF-driven undulator, in *Proc. of International Particle Accelerator Conference (IPAC'17), Copenhagen, Denmark, 14-19 May, 2017* (JACoW, Geneva, Switzerland, 2017), pp. 1643–1646.

[23] F. Toufexis, J. Neilson, and S. G. Tantawi, Coupling and polarization control in a mm-wave undulator, in *Proc. of International Particle Accelerator Conference (IPAC'17), Copenhagen, Denmark, 14-19 May, 2017* (JACoW, Geneva, Switzerland, 2017), pp. 1647–1650.

[24] T. Shintake *et al.*, Stable operation of a self-amplified spontaneous-emission free-electron laser in the extremely ultraviolet region, Phys. Rev. Accel. Beams **12**, 070701 (2009).

[25] K. L. Felch, B. G. Danly, H. R. Jory, K. E. Kreischer, W. Lawson, B. Levush, and R. J. Temkin, Characteristics and applications of fast-wave gyrodevices, Proc. IEEE **87**, 752 (1999).

[26] J. Neilson, L. Ives, M. Read, M. Mizuhara, D. Marsden, T. Robinson, J. Guevara, W. Lawson, and B. Hogan, W-band gyroklystron for high power RF applications, in *4th IEEE International Conference on Vacuum Electronics, 2003* (IEEE, Seoul, South Korea, 2003) pp. 346–347, https://ieeexplore-ieee-org.stanford.idm.oclc.org/abstract/document/1286376/.

[27] K. R. Chu, The electron cyclotron maser, Rev. Mod. Phys. **76**, 489 (2004).

[28] F. Toufexis, S. G. Tantawi, A. Jensen, V. A. Dolgashev, A. Haase, M. V. Fazio, and P. Borchard, Experimental demonstration of a 5th harmonic mm-wave frequency multiplying vacuum tube, Appl. Phys. Lett. **110**, 263507 (2017).

[29] V. Dolgashev, Beam powered RF undulator, Technical Report No. SLAC-PUB-17013, 2017, https://slac.stanford.edu/pubs/slacpubs/17000/slac-pub-17013.pdf.

[30] F. Toufexis, V. A. Dolgashev, C. Limborg-Deprey, and S. G. Tantawi, A compact EUV light source using a mm-wave undulator, in *Proc. of International Particle Accelerator Conference (IPAC'17), Copenhagen, Denmark, 14-19 May, 2017* (JACoW, Geneva, Switzerland, 2017), pp. 928–931.

[31] F. Toufexis, V. A. Dolgashev, C. Limborg-Deprey, and S. G. Tantawi, Compact linac-driven light sources utilizing mm-period RF undulators, in *Advances in Laboratory-based X-Ray Sources, Optics, and Applications VI*, edited by G. Pareschi and A. M. Khounsary (International Society for Optics and Photonics, San Diego, CA, 2017), p. 1038704, https://doi.org/10.1117/12.2274296.

[32] C. Limborg-Deprey, C. Adolphsen, D. McCormick, M. Dunning, K. Jobe, H. Li, T. Raubenheimer, A. Vrielink, T. Vecchione, F. Wang, and S. Weathersby, Performance of a first generation X-band photoelectron rf gun, Phys. Rev. Accel. Beams **19**, 053401 (2016).

[33] G. Schutz, W. Wagner, W. Wilhelm, P. Kienle, R. Zeller, R. Frahm, and G. Materlik, Absorption of Circularly Polarized x Rays in Iron, Phys. Rev. Lett. **58**, 737 (1987).

[34] C. E. Graves *et al.*, Nanoscale spin reversal by non-local angular momentum transfer following ultrafast laser excitation in ferrimagnetic GdFeCo, Nat. Mater. **12**, 293 (2013).

[35] D. J. Higley *et al.*, Femtosecond X-ray magnetic circular dichroism absorption spectroscopy at an X-ray free electron laser, Rev. Sci. Instrum. **87**, 033110 (2016).

[36] N. Bowering, T. Lischke, B. Schmidtke, N. Muller, T. Khalil, and U. Heinzmann, Asymmetry in Photoelectron Emission from Chiral Molecules Induced by Circularly Polarized Light, Phys. Rev. Lett. **86**, 1187 (2001).

[37] U. Hergenhahn, E. E. Rennie, O. Kugeler, S. Marburger, T. Lischke, I. Powis, and G. Garcia, Photoelectron circular dichroism in core level ionization of randomly oriented pure enantiomers of the chiral molecule camphor, J. Chem. Phys. **120**, 4553 (2004).

[38] L. A. Nguyen, H. He, and C. Pham-Huy, Chiral drugs: An overview, International Journal of Biomedical Science: IJBS **2**, 85 (2006).

[39] C. T. Chen, F. Sette, Y. Ma, and S. Modesti, Soft-x-ray magnetic circular dichroism at the $L_{2,3}$ edges of nickel, Phys. Rev. B **42**, 7262 (1990).

[40] P. Elleaume, Generation of various polarization states from insertion devices: A review, Rev. Sci. Instrum. **60**, 1830 (1989).

[41] O. A. Shevchenko, V. N. Litvinenko, S. M. Mikhailov, N. A. Vinokurov, N. G. Gavrilov, P. D. Vobly, and Y. Wu, The VUV/UV OK-5 duke storage ring FEL with variable polarization, in *PACS2001. Proceedings of the*

2001 Particle Accelerator Conference (Cat. No.01CH37268) (IEEE, New York, 2001), pp. 2833–2835, Vol. 4.

[42] E. Allaria *et al.*, Two-stage seeded soft-X-ray free-electron laser, Nat. Photonics **7**, 913 (2013).

[43] A. B. Temnykh, Delta undulator for Cornell energy recovery linac, Phys. Rev. Accel. Beams **11**, 120702 (2008).

[44] A. A. Lutman *et al.*, Polarization control in an X-ray free-electron laser, Nat. Photonics **10**, 468 (2016).

[45] B. Vodungbo, A. B. Sardinha, J. Gautier, G. Lambert, C. Valentin, M. Lozano, G. Iaquaniello, F. Delmotte, S. Sebban, J. Luning, and P. Zeitoun, Polarization control of high order harmonics in the EUV photon energy range, Opt. Express **19**, 4346 (2011).

[46] B. Pfau, C. Gunther, R. Konnecke, E. Guehrs, O. Hellwig, W. F. Schlotter, and S. Eisebitt, Magnetic imaging at linearly polarized x-ray sources, Opt. Express **18**, 13608 (2010).

[47] T. Wang *et al.*, Femtosecond Single-Shot Imaging of Nanoscale Ferromagnetic Order in Co/Pd Multilayers Using Resonant X-Ray Holography, Phys. Rev. Lett. **108**, 267403 (2012).

[48] J. L. Doane, Grating polarizers in waveguide miter bends, Int. J. Infrared Millim. Waves **13**, 1727 (1992).

[49] I. Stil, A. L. Fontana, B. Lefranc, A. Navarrini, P. Serres, and K. F. Schuster, Loss of WR10 waveguide across 70–116 GHz, in *Proc. 22nd Int. Symp. Space Terahertz Technol* (National Radio Astronomy Observatory, Tokyo, Japan, 2012), pp. 1–3, http://www.nrao.edu/meetings/isstt/papers/2012/2012151153.pdf.

[50] R. A. Olstad, J. L. Doane, and C. P. Moeller, Considerations in selection of ECH system transmission line waveguide diameter for ITER, J. Phys. Conf. Ser. **25**, 166 (2005).

[51] R. J. Wylde, Millimetre-wave Gaussian beam-mode optics and corrugated feed horns, IEE Proceedings H—Microwaves, Optics and Antennas **131**, 258 (1984).

[52] J. M. Neilson, P. E. Latham, M. Caplan, and W. G. Lawson, Determination of the resonant frequencies in a complex cavity using the scattering matrix formulation, IEEE Trans. Microwave Theory Techniques **37**, 1165 (1989).

[53] M. Shumail, Theory, design, and demonstration of a new microwave-based undulator, Ph.D. thesis, Stanford University, 2014.

[54] V. A. Dolgashev, High magnetic fields in couplers of X-band accelerating structures, in *Proceedings of the 2003 Particle Accelerator Conference, Portland, OR* (IEEE, New York, 2003), pp. 1267–1269 Vol. 2.

[55] L. Laurent, S. Tantawi, V. Dolgashev, C. Nantista, Y. Higashi, M. Aicheler, S. Heikkinen, and W. Wuensch, Experimental study of rf pulsed heating, Phys. Rev. Accel. Beams **14**, 041001 (2011).

[56] I. Zagorodnov and T. Weiland, TE/TM field solver for particle beam simulations without numerical Cherenkov radiation, Phys. Rev. Accel. Beams **8**, 042001 (2005).

[57] K. L. F. Bane, Wakefield effects in a linear collider, AIP Conf. Proc. **153**, 971 (1987), https://aip.scitation.org/doi/pdf/10.1063/1.36375.

[58] T. P. Wangler, *RF Linear Accelerators* (John Wiley & Sons, New York, 2008).

[59] J. M. Neilson, An improved multimode horn for Gaussian mode generation at millimeter and submillimeter wavelengths, IEEE Trans. Antennas Propag. **50**, 1077 (2002).

[60] R. S. Symons, H. R. Jory, S. J. Hegji, and P. E. FergusonAn experimental gyro-TWT, IEEE Trans. Microwave Theory Techniques **29**, 181 (1981).

[61] L. R. Barnett, L. H. Chang, H. Y. Chen, K. R. Chu, W. K. Lau, and C. C. Tu, Absolute Instability Competition And Suppression In A Millimeter-Wave Gyrotron Traveling-Wave Tube, Phys. Rev. Lett. **63**, 1062 (1989).

[62] J. Wang, Y. Luo, Y. Xu, R. Yan, Y. Pu, X. Deng, and H. Wang, Simulation and Experiment of a Ku-Band Gyro-TWT, IEEE Trans. Electron Devices **61**, 1818 (2014).

[63] T. Tanaka and H. Kitamura, SPECTRA: A synchrotron radiation calculation code, J. Synchrotron Radiat. **8**, 1221 (2001).

[64] T. Tanaka, Numerical methods for characterization of synchrotron radiation based on the Wigner function method, Phys. Rev. Accel. Beams **17**, 060702 (2014).

[65] T. Tanaka, Coherent mode decomposition using mixed Wigner functions of Hermite-Gaussian beams, Opt. Lett. **42**, 1576 (2017).